MEDICAL APPLICATIONS OF MICROWAVE IMAGING

Edited by
Lawrence E. Larsen
John H. Jacobi

Published under the sponsorship of the IEEE Microwave Theory and Techniques Society.

Supported by the U.S. Army Medical Research and Development Command.

Microwave Imaging with First Order Diffraction Tomography

Malcolm Slaney,* Mani Azimi,** Avinash C. Kak,*** and Lawrence E. Larsen****

Tomographic imaging with microwave radiation is discussed from the perspective of relating the Fourier transformation of projection views (both bistatic and monostatic) to samples of the two-dimensional Fourier transformation of the scattering object. The limitations of the first order Born and Rytov approximations in scalar diffraction tomography are explored. The role of a complex index of refraction for the coupling medium and/or target is emphasized.

1. INTRODUCTION

During the past ten years the medical community has increasingly called on X-Ray computerized tomography (CT) to help make its diagnostic images. With this increased interest has also come an awareness of the dangers of using ionizing radiation and this, for example, has made X-Ray CT unsuitable for use in mass screening for cancer detection in the female breast. As a result, in recent years much attention has been given to imaging with alternative forms of energy such as low-level microwaves, ultrasound and NMR (nuclear-magnetic-resonance). Ultrasonic B-scan imaging has already found widespread clinical applications; however it lacks the quantitative aspects of ultrasonic computed tomography, which in turn can only be applied to soft tissue structures such as the female breast.

A necessary attribute of any form of radiation used for biological imaging is that it be possible to differentiate between different tissues on the basis of local propagation parameters. It has already been demonstrated by Larsen and Jacobi in a companion paper elsewhere in this volume and in reference [1] that this condition is satisfied by microwave radiation with the relative dielectric constant and the electric loss factor in the 1–10 GHz range. When used for tomography, a distinct feature of microwaves is that they allow one to reconstruct cross-sectional images of the molecular properties of the object. The dielectric properties of the water molecule dominate the interaction of microwaves and biological systems [2], [3] and thus by interrogating the object with microwaves it is possible to image, for example, the state of hydration of an object.

The past interest in microwave imagery has focused primarily on either the holographic, or the pulse-echo modes. In the holographic mode, most attention has focussed on conducting targets in air, such as that described elsewhere in this volume by Farhat. There are exceptions as represented by the work of Yue et al. [4] wherein low-dielectric-constant slabs embedded in earth were imaged. The approach of Yue et al. is not applicable to the cross-sectional imaging of complicated three-dimensional objects, because of the underlying assumptions made regarding the availability of a priori information about the "propagators" in a volume cell of the object. Another example of microwave imaging with holography is the work of Gregoris and Izuka [5], wherein conductors and planar dielectric voids were holographically imaged inside flat dielectric layers. A reflection from the air-dielectric interface provided the reference beam. Again this work is not particularly relevant for microwave imaging of biosystems since many important biological constituents are dielectrics dominated by water. When used in the pulse-echo mode, microwaves again possess limited usefulness due to the requirement that the object be in the far field of the transmit/receive aperture, although the video pulse technique, described by Kim & Webster elsewhere in the volume mitigate this objection to some extent.

Tomography represents an attractive alternative to both holography and pulse-echo for cross-sectional (or three-dimensional) reconstruction of geometrically complicated biosystems, but there is a fundamental difference between tomographic imaging with x-rays and microwaves. X-rays, being non-diffracting, travel in straight lines, and therefore, the transmission data measures the line integral of some object parameter along straight lines. This makes it possible to apply the Fourier-slice theorem [6], which says that the

* Malcolm Slaney was with the School of Electrical Engineering, Purdue University, West Lafayette, IN 47907. He is now with Schlumberger Palo Alto Research, 3340 Hillview Avenue, Palo Alto, CA 94304.
** Mani Azimi was with the School of Electrical Engineering, Purdue University, West Lafayette, IN 47907. He is now with Department of Electrical Engineering, Michigan State University, East Lansing, MI 48824.
*** Avinash C. Kak is with the School of Electrical Engineering, Purdue University, West Lafayette, IN 47907.
**** Lawrence E. Larsen is with Microwaves Department, Walter Reed Army Institute of Research, Washington, DC 20012.

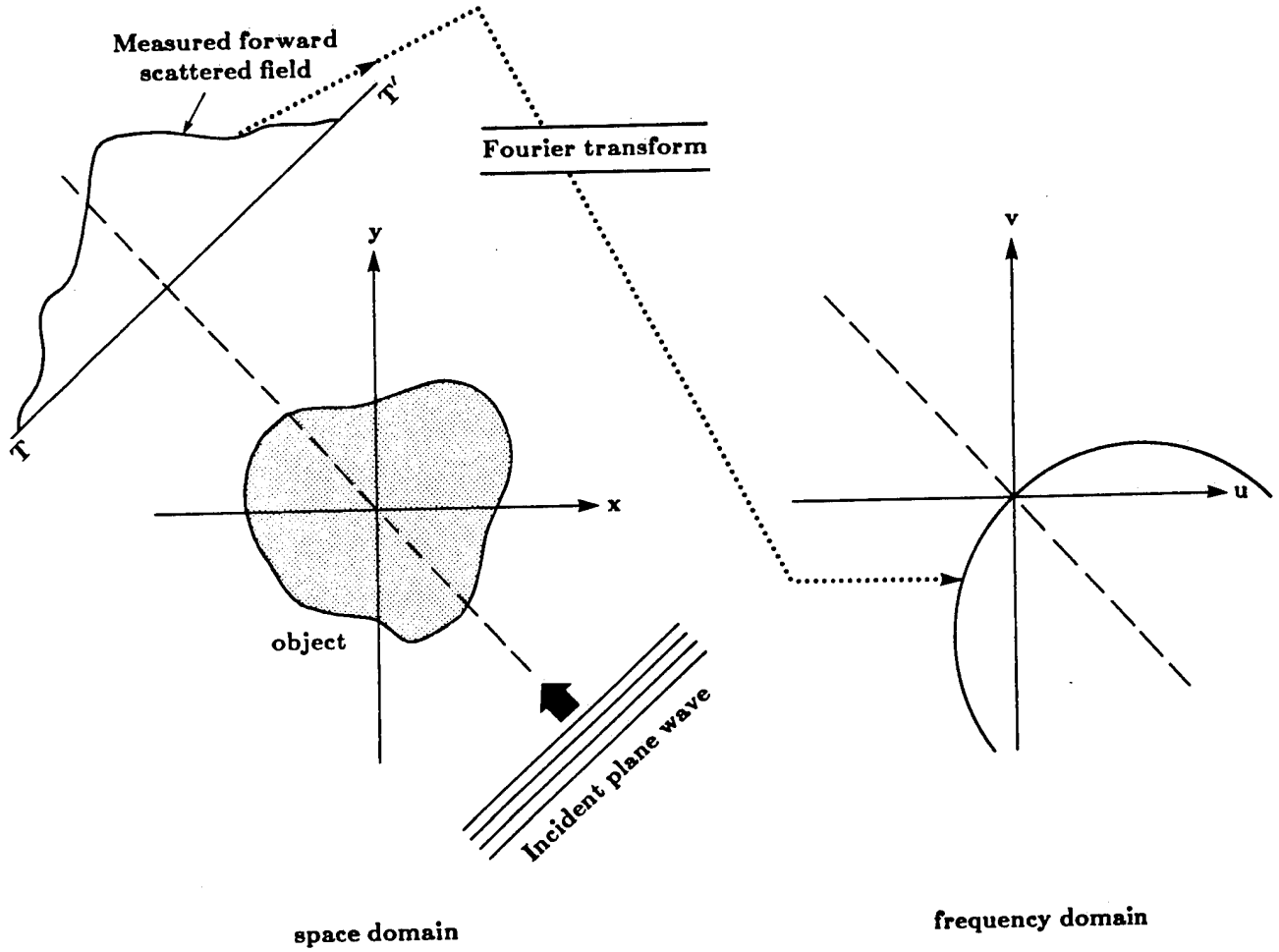

Fig. 1. The Fourier Diffraction Theorem.

Fourier transform of a projection is equal to a slice of the two-dimensional Fourier transform of the object.

On the other hand, when microwaves are used for tomographic imaging, the energy often does not propagate along straight lines. When the object inhomogeneities are large compared to a wavelength, energy propagation is characterized by refraction and multipath effects. Moderate amounts of ray bending induced by refraction can be taken into account by combining algebraic reconstruction algorithms [7] with digital ray tracing and ray linking algorithms [8].

When the object inhomogeneities become comparable in size to a wavelength, it is not even appropriate to talk about propagation along lines or rays, and energy transmission must be discussed in terms of wavefronts and fields scattered by the inhomogeneities. Polarization or vector fields must also be considered in this circumstance as discussed in a review article on inverse scattering by Boerner and Chan elsewhere in this volume. A tutorial presentation of polarization description and polarimetric imaging is in a companion paper by Larsen & Jacobi elsewhere in this volume. When consideration is limited to scalar fields, it has been shown [9], [10], [11], [12] that with certain approximations a Fourier-slice like theorem can be formulated. In [13] this theorem was called the Fourier Diffraction Projection Theorem. It may simply be stated as follows:

> When an object is illuminated with a plane wave as shown in Fig. 1, the Fourier transform of the forward scattered fields measured on a line perpendicular to the direction of propagation of the wave (line TT in Fig. 1) gives the values of the 2-D Fourier transform of the object along a circular arc as shown in the figure.

In Section 2 we will review the proof of this theorem. In our review, we will show how the derivation of the theorem points to a FFT-based implementation of higher order Born and Rytov algorithms, which are currently under development by us and other researchers. *The Fourier Diffraction Projection Theorem is valid only when the inhomogeneities in the object are weakly scattering.*

According to the Fourier Diffraction Projection Theorem, by illuminating an object from many different directions and measuring the diffracted data, one can in principle fill up the Fourier space with the samples of the Fourier transform of

the object over an ensemble of circular arcs and then reconstruct the object by Fourier inversion.

The above theorem forms the basis of first order diffraction tomography. The work of Mueller et al. [11] was initially responsible for focusing the attention of many researchers on this approach to cross-sectional and three-dimensional imaging, although from a purely scientific standpoint the technique owes its origins to the now classic paper by Wolf [12], and a subsequent article by Iwata and Nagata [14].

This chapter will review the theory, implementation and some of the mathematical limitations of diffraction tomography with microwaves. As will be shown in the review of Section 2, the algorithms for diffraction tomography are derived from the classical wave equation. The wave equation is a non-linear differential equation that relates an object to the surrounding fields. To estimate a cross-sectional iamge of an object, it is necessary to find a linear solution to the wave equation and then to invert this relation between the object and the scattered field. The necessary approximations for this purpose limit the range of objects that can be successfully imaged to those that do not severely change the incident field or have a small refractive index gradient compared to the surrounding media.

In Section 3 we will look at several different methods to collect the scattered data and then invert it to find an estimate of the object. To generate a good estimate of the object it is necessary to combine the information from a number of different fields and this can be done with several different approaches. Then a simple algorithm based on the Fourier Diffraction Projection Theorem can be used to invert the scattered data.

Finally in Section 4 we will show the effects of these approximations by calculating the scattered fields for computer simulated objects using a number of different approaches. For cylindrical objects with a single refractive index it is possible to use the boundary conditions to solve for the exact scattered field. These simulations will establish the first order Born approximation to be valid for objects where the product of the change in refractive index and the diameter is less than 0.35λ and the first order Rytov approximation for changes in the refractive index of less than a few percent, with essentially no constraint on the object size. The scattered fields from objects that consist of more than one cylindrical object will then be calculated using Twersky's multiple scattering theory. These simulations will show that even when each component of the object satisfies the Born approximation the multiple scattering can degrade the reconstruction. Finally simulations will show that when attenuation is included in the model the high frequency information about the object is lost.

2. THE FOURIER DIFFRACTION THEOREM

Diffraction tomography is based on a linear solution to the wave equation. The wave equation relates an object and the scattered field and by linearizing it we can find an estimate of a cross section of the object based on the scattered field. The approximations used in the linearization process are crucial to the success of diffraction tomography and we will be careful to highlight the assumptions.

2.1 The Wave Equation

In a homogeneous medium, electromagnetic waves, $\psi(\vec{r})$, satisfy a homogeneous wave equation of the form

$$(\nabla^2 + k_0^2)\psi(\vec{r}) = 0, \tag{1}$$

where the wave number, k_0, represents the spatial frequency of the plane wave and is a function of the wavelength, λ, or $k_0 = 2\pi/\lambda$. It is easy to verify that a solution to Eq. (1) is given by a plane wave

$$\psi(\vec{r}) = e^{i\vec{k}_0\cdot\vec{r}} \tag{2}$$

where $\vec{k}_0 = (k_x, k_y)$ is the wave vector of the wave and satisfies the relation $|\vec{k}_0| = k_0$. For imaging, an inhomogeneous medium is of interest, so the more general form of the wave equation is written as

$$(\nabla^2 + k^2(\vec{r}))\psi(\vec{r}) = 0. \tag{3}$$

For electromagnetic fields, if the effects of polarization are ignored, $k(\vec{r})$ can be considered to be a scalar function representing the refractive index of the medium. We then write

$$k(\vec{r}) = k_0 n(\vec{r}) = k_0[1 + n_\delta(\vec{r})], \tag{4}$$

where k_0 now represents the average wavenumber of the media, and $n(\vec{r})$ is the refractive index as given by

$$n(\vec{r}) = \sqrt{\frac{\mu(\vec{r})\epsilon(\vec{r})}{\mu_0\epsilon_0}}. \tag{5}$$

The parameter $n_\delta(\vec{r})$ represents the deviation from the average of the refractive index. In general it will be assumed that the object of interest has finite support so $n_\delta(\vec{r})$ is zero outside the object. Here we have used μ and ϵ to represent the magnetic permeability and dielectric constant and the subscript zero to indicate their average values.

If the second order terms in n_δ (i.e., $n_\delta \ll 1$) are ignored we find

$$(\nabla^2 + k_0^2)\psi(\vec{r}) = -2k_0^2 n_\delta(\vec{r})\psi(\vec{r}) = -\psi(\vec{r})O(\vec{r}), \tag{6}$$

where $O(\vec{r}) = 2k_0^2 n_\delta(\vec{r})$ is usually called the object function.

Note that Eq. (6) is a *scalar* wave propagation equation. Its use implies that there is no depolarization as the electromagnetic wave propagates through the medium. It is known [15] that the depolarization effects can be ignored only if the wavelength is much smaller than the correlation size of the inhomogeneities in the object. If this condition is not satisfied, then strictly speaking the following vector wave propagation equation must be used:

$$\nabla^2\vec{E}(r) + k_0^2 n^2\vec{E}(\vec{r}) - 2\nabla\left[\frac{\nabla n}{n}\cdot\vec{E}\right] = 0, \tag{7}$$

where $\vec{E}$ is the electric field vector. A vector theory for diffraction tomography based on this equation has yet to be developed.

In addition $\psi_0(\vec{r})$, the incident field, may be defined as

$$(\nabla^2 + k_0^2)\psi_0(\vec{r}) = 0. \tag{8}$$

Thus $\psi_0(\vec{r})$ represents the source field or the field present without any object inhomogeneities. The total field then is expressed as the sum of the incident field and the scattered field

$$\psi(\vec{r}) = \psi_0(\vec{r}) + \psi_s(\vec{r}), \tag{9}$$

with ψ_s satisfying the wave equation

$$(\nabla^2 + k_0^2)\psi_s(\vec{r}) = -\psi(\vec{r})O(\vec{r}) \tag{10}$$

which is obtained by substituting Eqs. (8) and (9) in Eq. (6). This form of the wave equation will be used in the work to follow.

The scalar Helmholtz equation (10) cannot be solved for $\psi_s(\vec{r})$ directly but a solution can be written in terms of a Green's function [16]. The Green's function, which is a solution of the differential equation

$$(\nabla^2 + k_0^2)G(\vec{r}|\vec{r}') = -\delta(\vec{r} - \vec{r}'), \tag{11}$$

is written in 3-space as

$$G(\vec{r}|\vec{r}') = \frac{e^{jk_0R}}{4\pi R}, \tag{12}$$

with

$$R = |\vec{r} - \vec{r}'|. \tag{13}$$

In two dimensions, the solution of (11) is written in terms of a zero-order Hankel function of the first kind, and can be expressed as

$$G(\vec{r}|\vec{r}') = \frac{j}{4} H_0^{(1)}(k_0R). \tag{14}$$

In both cases the Green's function, $G(\vec{r}|\vec{r}')$, is only a function of the difference $\vec{r} - \vec{r}'$ so the argument of the Green's function will often be represented as simply $G(\vec{r} - \vec{r}')$. Because the object function in Eq. (11) represents a point inhomogeneity, the Green's function can be considered to represent the field resulting from a single point scatterer.

Since Eq. (11) represents the radiation from a two-dimensional impulse source, the total radiation from all sources on the right hand side of (10) must be given by the following superposition:

$$\psi_s(\vec{r}) = \int G(\vec{r} - \vec{r}')O(\vec{r}')\psi(\vec{r}')d\vec{r}'. \tag{15}$$

In general, it is impossible to solve Eq. (15) for the scattered field, so approximations must be made. Two types of approximations will be considered: the Born and the Rytov.

2.2 The Born Approximation

The Born approximation is the simpler of the two approaches. Consider the total field, $\psi(\vec{r})$, expressed as the sum of the incident field, $\psi_0(\vec{r})$, and a small perturbation, $\psi_s(\vec{r})$, as in Eq. (9). The integral of Eq. (15) is now written as

$$\psi_s(\vec{r}) = \int G(\vec{r} - \vec{r}')O(\vec{r}')\psi_0(\vec{r}')d\vec{r}' + \int G(\vec{r} - \vec{r}')O(\vec{r}')\psi_s(\vec{r}')d\vec{r}'. \tag{16}$$

If the scattered field, $\psi_s(\vec{r})$, is small compared to $\psi_0(\vec{r})$, the effects of the second integral can be ignored to arrive at the approximation

$$\psi_s(\vec{r}) = \int G(\vec{r} - \vec{r}')O(\vec{r}')\psi_0(\vec{r}')d\vec{r}'. \tag{17}$$

This constitutes the first-order Born approximation. For a moment, let's denote the scattered fields obtained in this manner by $\psi_s^{(1)}(\vec{r})$. If one wished to compute $\psi_s^{(2)}(\vec{r})$ which represents the second order approximation to the scattered fields, that could be accomplished by substituting $\psi_0 + \psi_s^{(1)}$ for ψ_0 in the right hand side of Eq. (17), yielding

$$\psi_s^{(2)}(\vec{r}) = \int G(\vec{r} - \vec{r}')O(\vec{r}')[\psi_0(\vec{r}') + \psi_s^{(1)}(\vec{r}')]d\vec{r}'. \tag{18}$$

In general, we may write

$$\psi_s^{(i+1)}(\vec{r}) = \int G(\vec{r} - \vec{r}')O(\vec{r}')[\psi_0(\vec{r}') + \psi_s^{(i)}(\vec{r}')]d\vec{r}' \tag{19}$$

for the higher (i + 1)'th approximation to the scattered fields in terms of the i'th solution. Since the science of reconstructing objects with higher order approximations is not fully developed, this particular point will not be pursued any further and the first order scattered fields will be represented by ψ_s (i.e., without the superscript).

Note again that the first-order Born approximation is valid only when the magnitude of the scattered field,

$$\psi_s(\vec{r}) = \psi(\vec{r}) - \psi_0(\vec{r}), \tag{20}$$

is smaller than that of the incident field, ψ_0. If the object is a cylinder of constant refractive index it is possible to express this condition as a function of the size of the object (radius = a) and the refractive index. Let the incident wave, $\psi_0(\vec{r})$, be a plane wave propagating in the direction of the unit vector, $\vec{k}_0$. For a large object, the field inside the object will not be given by

$$\psi(\vec{r}) = \psi_{object}(\vec{r}) \neq Ae^{j\vec{k}_0\cdot\vec{r}}, \tag{21}$$

but instead will be a function of the change in refractive index, n_δ. Along a ray through the center of the cylinder and parallel to the direction of propagation of the incident plane wave, the field inside the object becomes a slow (or fast) version of the incident wave or

$$\psi_{object}(\vec{r}) = Ae^{j(1+n_\delta)\vec{k}_0\cdot\vec{r}}. \tag{22}$$

Since the wave is propagating through the object, the phase difference between the incident field and the field inside the object is approximately equal to the integral through the object of the change in refractive index. Therefore, for a cylinder the total phase shift through the object is approximately

$$\text{Phase Change} = 4\pi n_\delta \frac{a}{\lambda}, \tag{23}$$

where λ is the wavelength of the incident wave. For the

first-order Born approximation to be valid, a necessary condition is that the change in phase between the incident field and the wave propagating through the object be less than π. This condition can be expressed mathematically as

$$n_\delta a < \frac{\lambda}{4}. \tag{24}$$

2.3 The Rytov Approximation

The Rytov approximation is valid under slightly less severe restrictions. It is derived by considering the total field to be represented as [15]

$$\psi(\vec{r}) = e^{\phi(\vec{r})}, \tag{25}$$

and rewriting the wave Eq. (1) as

$$(\nabla\phi)^2 + \nabla^2\phi + k_0^2 = -2k_0^2 n_\delta. \tag{26}$$

Expressing the total phase, ϕ, as the sum of the incident phase function ϕ_0 and the scattered complex phase ϕ_s or

$$\phi(\vec{r}) = \phi_0(\vec{r}) + \phi_s(\vec{r}), \tag{27}$$

where

$$\psi_0(\vec{r}) = e^{\phi_0(\vec{r})}, \tag{28}$$

we find that

$$(\nabla\phi_0)^2 + 2\nabla\phi_0\cdot\nabla\phi_s + (\nabla\phi_s)^2 + \nabla^2\phi_0 + \nabla^2\phi_s + k_0^2(1 + 2n_\delta) = 0. \tag{29}$$

As in the Born approximation, it is possible to set the zero perturbation equation equal to zero to find

$$2\nabla\phi_0\cdot\nabla\phi_s + \nabla^2\phi_s = -(\nabla\phi_s)^2 - 2k_0^2 n_\delta. \tag{30}$$

This equation is inhomogeneous and nonlinear but can be linearized by considering the following relation

$$\nabla^2(\psi_0\phi_s) = \nabla^2\psi_0\cdot\phi_s + 2\nabla\psi_0\cdot\nabla\phi_s + \psi_0\nabla^2\phi_s. \tag{31}$$

Recalling that

$$\psi_0 = Ae^{j\vec{k}_0\cdot\vec{r}} = e^{\phi_0(\vec{r})}, \tag{32}$$

we find

$$2\psi_0\nabla\phi_0\cdot\nabla\phi_s + \psi_0\nabla^2\phi_s = \nabla^2(\psi_0\phi_s) + k_0^2\psi_0\phi_s. \tag{33}$$

This result can be substituted into Eq. (30) to find

$$(\nabla^2 + k_0^2)\psi_0\phi_s = -\psi_0[(\nabla\phi_s)^2 + 2k_0^2 n_\delta]. \tag{34}$$

As before, the solution to this differential equation can again be expressed as an integral equation. This becomes

$$\psi_0\phi_s = \int_{V'} G(\vec{r} - \vec{r}')\psi_0[(\nabla\phi_s)^2 + 2k_0^2 n_\delta]dr', \tag{35}$$

where the Green's function is given by (14).

Under the Rytov approximation, it is assumed that the term in brackets in the above equation can be approximated by

$$(\nabla\phi_s)^2 + 2k_0^2 n_\delta \simeq 2k_0^2 n_\delta. \tag{36}$$

When this is done the first-order Rytov approximation to the scattered phase, ϕ_s, becomes

$$\phi_s(\vec{r}) \simeq \frac{2}{\psi_0(\vec{r})}\int_{V'} G(\vec{r} - \vec{r}')\psi_0(\vec{r})k_0^2 n_\delta dr'. \tag{37}$$

Substituting the expression for ψ_s given in Eq. (17) yields

$$\phi_s(\vec{r}) \simeq \frac{\psi_s(\vec{r})}{\psi_0(\vec{r})}. \tag{38}$$

It is important to note that, in spite of the similarity of the Born (17) and the Rytov (37) solutions, the approximations are quite different. As will be seen later, the Born approximation produces a better estimate of the scattered fields for objects small in size with large deviations in the refractive index. On the other hand, the Rytov approximation gives a more accurate estimate of the scattered field for large sized objects with small deviations in refractive index.

When the object is small and the refractive index deviates only slightly from the surrounding media, it is possible to show that the Born and the Rytov approximations produce the same results. Consider our definition of the scattered phase in Eq. (25) and (27). Expanding the scattered phase in the exponential with the Rytov solution to the scattered field, it is seen

$$\psi(\vec{r}) = e^{\phi_0(\vec{r})+\phi_s(\vec{r})} = \psi_0(\vec{r})e^{\exp(-j\vec{k}_0\cdot\vec{r})\psi_s(\vec{r})}. \tag{39}$$

For very small $\psi_s(\vec{r})$, the first exponential can be written in terms of the power series expansion to find

$$\psi(\vec{r}) \simeq \psi_0(\vec{r})[1 + \exp(-j\vec{k}_0\cdot\vec{r})\psi_s(\vec{r})] = \psi_0(\vec{r}) + \psi_s(\vec{r}). \tag{40}$$

Thus when the magnitude of the scattered field is very small the Rytov approximation simplifies to the Born approximation.

The Rytov approximation is valid under a less restrictive set of conditions than the Born approximation [17], [18]. In deriving the Rytov approximation, the assumption was made that

$$(\nabla\phi_s)^2 + 2k_0^2 n_\delta \simeq 2k_0^2 n_\delta. \tag{41}$$

Clearly this is true only when

$$n_\delta \gg \frac{(\nabla\phi_s)^2}{k_0^2}. \tag{42}$$

This can be justified by observing that to a first approximation the scattered phase, ϕ_s, is linearly dependent on n_δ [17]. If n_δ is small, then

$$(\nabla\phi_s)^2 \propto n_\delta^2 \tag{43}$$

will be even smaller and therefore the first term in Eq. (41) above can be safely ignored. *Unlike the Born approximation, the size of the object is not a factor in the Rytov approximation.* The term $\nabla\phi_s$ is the change in the complex scattered phase per unit distance and by substituting $k_0 = 2\pi/\lambda$ we find a necessary condition for the validity of the Rytov approximation is

$$n_\delta \gg \left[\frac{\nabla\phi_s\lambda}{2\pi}\right]^2. \tag{44}$$

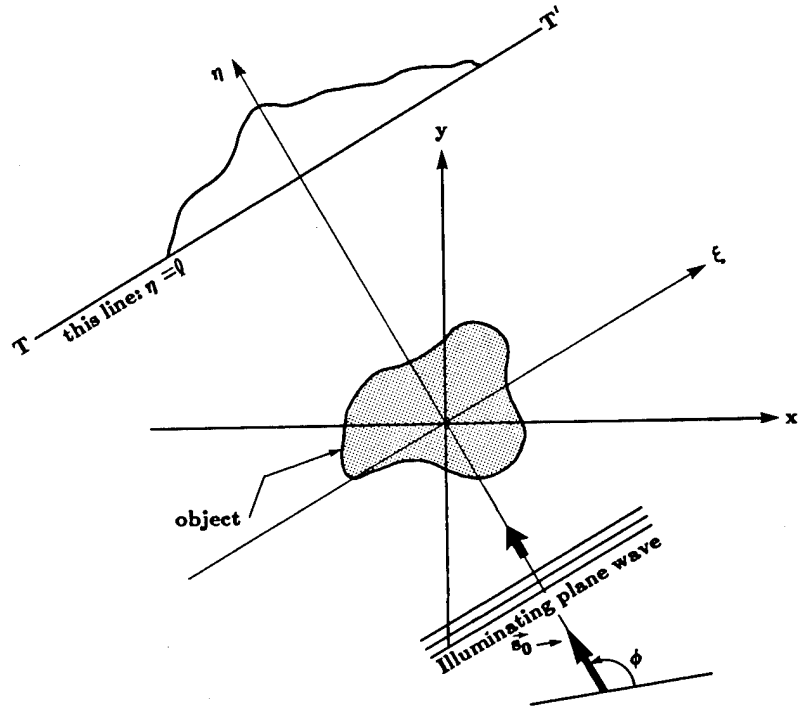

Fig. 2. A typical diffraction tomography experiment.

Therefore in the Rytov approximation, it is the change in scattered phase, ϕ_s, over one wavelength that is important and not the total phase. Thus, because of the ∇ operator the Rytov approximation is valid when the phase change over a single wavelength is small.

2.4 The Scattered Fields

The Fourier Diffraction Theorem relates the Fourier transform of the scattered field, the diffracted projection, to the Fourier transform of the object along a circular arc. While a number of researchers have derived this theory [11], [9], [13], [19] we would like to propose a system theoretic analysis of this result which is fundamental to first order diffraction tomography. This approach is superior not only because it allows the scattering process to be visualized in the Fourier domain but also because it points to efficient FFT-based computer implementations of higher order Born and Rytov algorithms currently under development. Since it appears that the higher order algorithms will be more computationally intensive, any savings in the computing effort involved is potentially important.

Consider the effect of a single plane wave incident on an object. The forward scattered field will be measured at a receiver line as shown in Fig. 2. We will find an expression for the field scattered by the object, $O(\vec{r})$, by analyzing Eq. (17) in the Fourier domain. We will use the plots of Fig. 3 to illustrate the transformations that take place.

The first Born equation for the scattered field (17) can be considered as a convolution of the Green's Function, $G(\vec{r})$, and the product of the object function, $O(\vec{r})$, and the incident field, $\psi_0(\vec{r})$. First we will define the following Fourier transform pairs:

$$\begin{aligned} O(\vec{r}) &\leftrightarrow \tilde{O}(\vec{\Lambda}), \\ G(\vec{r}) &\leftrightarrow \tilde{G}(\vec{\Lambda}) \end{aligned} \tag{45}$$

and

$$\psi(\vec{r}) \leftrightarrow \tilde{\psi}(\vec{\Lambda}),$$

where we have used the relationships

$$\tilde{O}(\vec{\Lambda}) = \int\int O(\vec{r}) e^{-j\vec{\Lambda}\cdot\vec{r}} d\vec{r}, \tag{46}$$

$\vec{\Lambda} = (\alpha,\beta)$ and (α,β) being the spatial angular frequencies along the x and y directions respectively.

The integral solution to the wave Eq. (17) can now be written in terms of these Fourier transforms

$$\tilde{\psi}_s(\vec{\Lambda}) = \tilde{G}(\vec{\Lambda})\{\tilde{O}(\vec{\Lambda}) * \tilde{\psi}_0(\vec{\Lambda})\}, \tag{47}$$

where we have used "$*$" to represent convolution. When the illumination field, ψ_0, consists of a single plane wave

$$\psi_0(\vec{r}) = e^{j\vec{k}_0\cdot\vec{r}} \tag{48}$$

with $\vec{k}_0 = (k_x,k_y)$ satisfying the following relationship

$$k_0^2 = k_x^2 + k_y^2 \tag{49}$$

its Fourier transform is given by

$$\tilde{\psi}_0(\vec{\Lambda}) = 2\pi\delta(\vec{\Lambda} - \vec{k}_0). \tag{50}$$

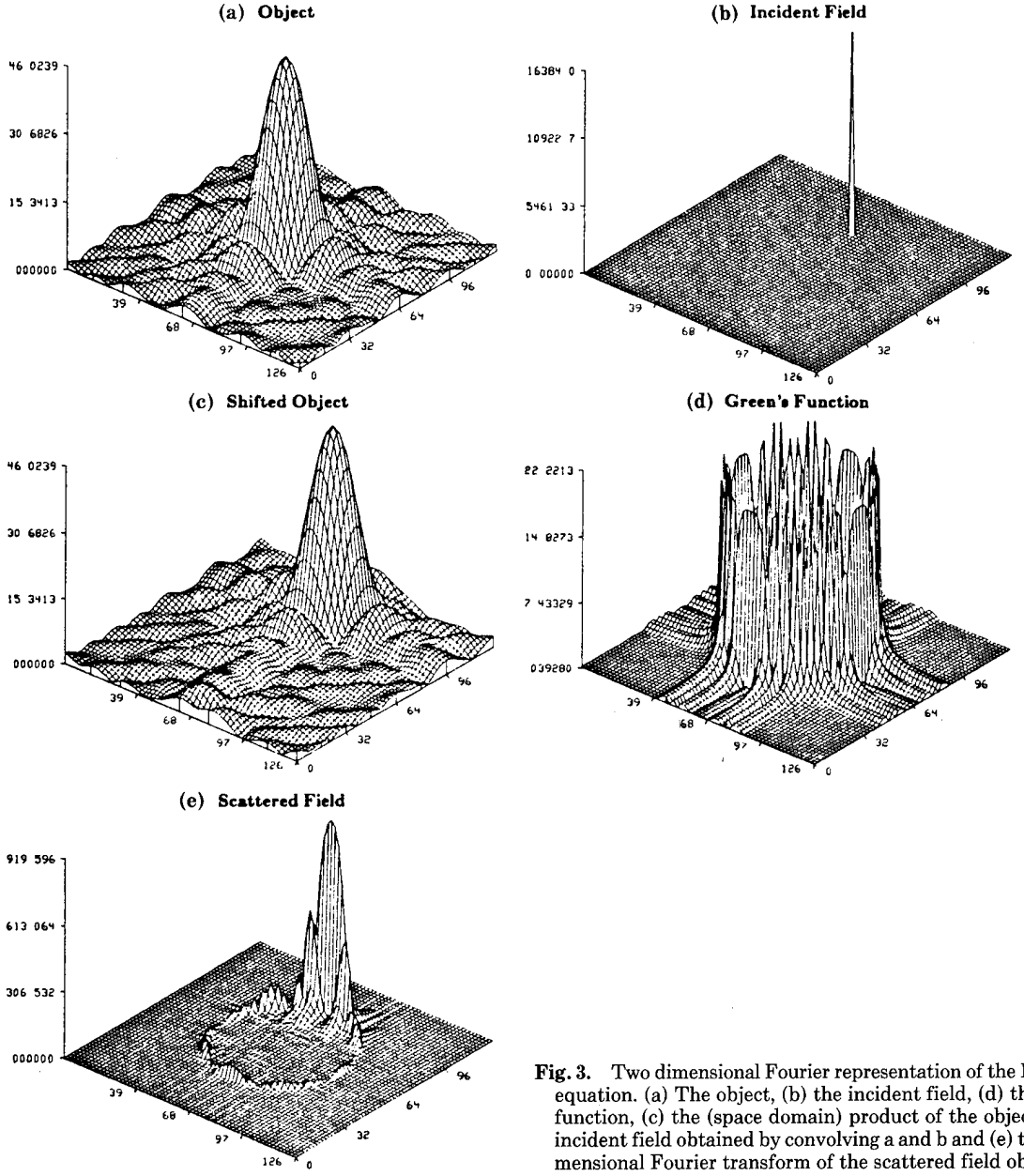

Fig. 3. Two dimensional Fourier representation of the Helmholtz equation. (a) The object, (b) the incident field, (d) the Green's function, (c) the (space domain) product of the object and the incident field obtained by convolving a and b and (e) the two dimensional Fourier transform of the scattered field obtained by multiplication of c and d.

The delta function causes the convolution of Eq. (47) to become a shift in the frequency domain as given by

$$\tilde{O}(\vec{\Lambda}) * \tilde{\psi}_0(\vec{\Lambda}) = 2\pi \tilde{O}(\vec{\Lambda} - \vec{k}_0). \tag{51}$$

This convolution is illustrated in Figs. 3a–c for a plane wave propagating with direction vector, $\vec{k}_0 = (0, k_0)$. Figure 3a shows the Fourier transform of a single cylinder of radius 1λ and Fig. 3b is the Fourier transform of the incident field. The resulting convolution in the frequency domain (or multiplication in the space domain) is shown in Fig. 3c.

To find the Fourier transform of the Green's function, the Fourier transform of Eq. (11) is taken to find

$$(-\Lambda^2 + k_0^2)\tilde{G}(\vec{\Lambda}|\vec{r}') = -e^{-j\vec{\Lambda}\cdot\vec{r}'}, \tag{52}$$

where $\Lambda^2 = \alpha^2 + \beta^2$. Rearranging terms we see that

$$\tilde{G}(\vec{\Lambda}|\vec{r}') = \frac{e^{-j\vec{\Lambda}\cdot\vec{r}'}}{\Lambda^2 - k_0^2}, \tag{53}$$

which has a singularity for all $\vec{\Lambda}$ such that

$$\Lambda^2 = \alpha^2 + \beta^2 = k_0^2. \tag{54}$$

In the space domain the two dimensional Green's function, Eq. (14), has a singularity at the origin so it is necessary to approximate the Green's function by using a two dimensional average of the values of the Green's function near the singularity. An approximation to $\tilde{G}(\vec{\Lambda})$ is shown in Fig. 3d.

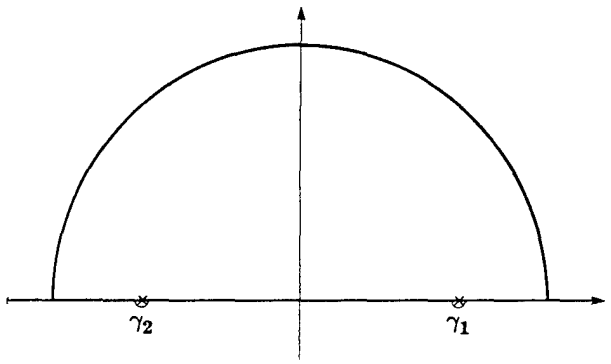

Fig. 4. Integration path in the complex plane for inverting the two dimensional Fourier transform of the scattered field.

The Fourier representation in Eq. (53) is misleading because both point sources and point sinks are valid solutions to Eq. (52). Thus the simple expression of Eq. (53) includes the effects of both waves moving toward and waves moving away from the point at $\vec{r}'$. Later, when we move back from the Fourier domain to the space domain, it will be necessary to choose the proper Fourier components so that only waves traveling away from the point scatterer are retained.

The effect of the convolution shown in Eq. (17) is a multiplication in the frequency domain of the shifted object function, Eq. (51), and the Green's function, Eq. (53), evaluated at $\vec{r}' = 0$. The scattered field is written as

$$\tilde{\psi}_s(\vec{\Lambda}) = 2\pi \frac{\tilde{O}(\vec{\Lambda} - \vec{k}_0)}{\Lambda^2 - k_0^2} . \tag{55}$$

This result is shown in Fig. 3e for a plane wave propagating along the y-axis. Since the largest frequency domain components of the Green's function satisfy Eq. (1), the Fourier transform of the scattered field is dominated by a shifted and sampled version of the object's Fourier transform.

We will now derive an expression for the field at the receiver line. For simplicity it will be assumed that the incident field is propagating along the positive y axis or $\vec{k}_0 = (0,k_0)$. The scattered field along the receiver line $(x,y = l_0)$ is simply the inverse Fourier transform of the field in Eq. (55). This is written as

$$\psi_s(x,y = l_0) = \frac{1}{4\pi^2} \int\int \tilde{\psi}_s(\vec{\Lambda}) e^{j\vec{\Lambda}\cdot\vec{r}} d\alpha d\beta, \tag{56}$$

which, using Eq. (55), can be expressed as

$$\psi_s(x,y = l_0) = \frac{1}{2\pi} \iint \frac{\tilde{O}(\alpha,\beta - k_0)}{\alpha^2 + \beta^2 - k_0^2} e^{j(\alpha x + \beta l_0)} d\alpha d\beta. \tag{57}$$

We will integrate with respect to β. For a given α, the integral has a singularity at

$$\beta_{1,2} = \pm \sqrt{k_0^2 - \alpha^2} . \tag{58}$$

Using contour integration we can close the integration path at infinity and evaluate the integral with respect to β along the path shown in Fig. 4 to find

$$\psi_s(x,l_0) = \int \Gamma_1(\alpha;l_0) e^{j\alpha x} d\alpha + \int \Gamma_2(\alpha;l_0) e^{j\alpha x} d\alpha, \tag{59}$$

where

$$\Gamma_1 = \frac{\tilde{O}(\alpha, \sqrt{k_0^2 - \alpha^2} - k_0)}{j2\sqrt{k_0^2 - \alpha^2}} e^{j\sqrt{k_0^2 - \alpha^2} l_0} \tag{60}$$

and

$$\Gamma_2 = \frac{\tilde{O}(\alpha, -\sqrt{k_0^2 - \alpha^2} - k_0)}{-j2\sqrt{k_0^2 - \alpha^2}} e^{j\sqrt{k_0^2 - \alpha^2} l_0}. \tag{61}$$

Examining the above pair of equations, it is seen that Γ_1 represents the solution in terms of plane waves traveling along the positive y axis while Γ_2 represents plane waves traveling in the $-y$ direction. These distinct solutions represent the two solutions to the wave equation for a point discontinuity [see Eq. (53)]. In both cases, as α ranges from $-k_0$ to k_0, Γ represents the Fourier transform of the object along a semicircular arc.

Since we are interested in the forward traveling waves, only the plane waves represented by the Γ_1 solution are valid; and, thus, the scattered field becomes

$$\psi_s(x,l_0) = \int \Gamma_1(\alpha;y) e^{j\alpha x} d\alpha \quad l_0 > \text{object} \tag{62}$$

where we have chosen the value of the square root to lead only to outgoing waves.

Taking the Fourier transform of both sides of Eq. (62) we find that

$$\int \psi_s(x,y = l_0) e^{-j\alpha x} dx = \tilde{\Gamma}(\alpha,l_0). \tag{63}$$

But since $\Gamma(x,l_0)$ is equal to a phase shifted version of the object function, the Fourier transform of the scattered field along the line $y = l_0$ is related to the Fourier transform of the object along a circular arc. The use of the contour integration is further justified by noting that only those waves that satisfy the relationship

$$\alpha^2 + \beta^2 = k_0^2 \tag{64}$$

will be propagated. Thus it is safe to ignore all waves not on the k_0-circle.

This result is diagramed in Fig. 5. The circular arc repre-

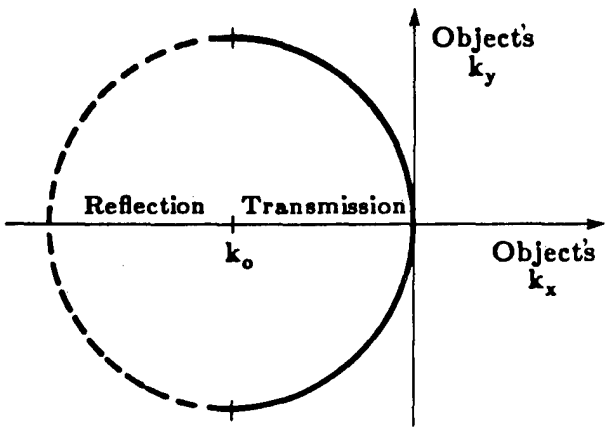

Fig. 5. Estimate of the two dimensional Fourier transform of the object are available along the solid arc for transmission tomography and the dashed arc for reflection tomography.

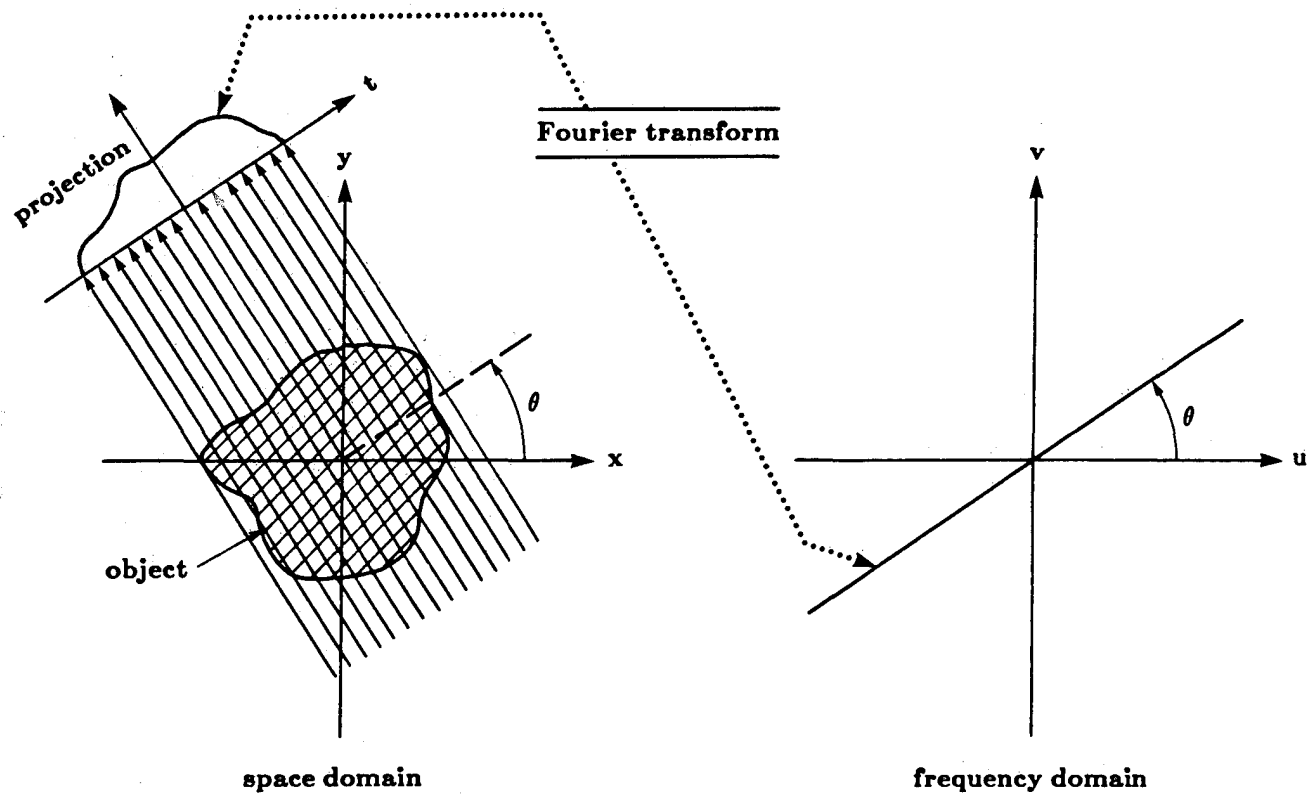

Fig. 6. The Fourier transform of a projection is equal to the two dimensional Fourier transform of the object along a radial line.

sents the locus of all points (α,β) such that $\beta = \pm\sqrt{k_0^2 - \alpha^2}$. The solid line shows the outgoing waves for a receiver line at $y = l_0$ greater than the object. This can be considered transmission tomography. Conversely the dashed line indicates the locus of solutions for $y = l_0$ less than the object or the reflection tomography case.

Straight-ray (i.e., X-ray) tomography is based on the Fourier Slice Theorem [10], [6]

> The Fourier transform of a parallel projection of an image f(x,y) taken at an angle θ gives a slice of the 2-D transform, $F(\omega_1,\omega_2)$ subtending an angle θ with the ω_1 axis.

This is diagramed in Fig. 6.

Equation (63) leads us to a similar result for diffraction tomography. Recall that α and β in Eq. (63) are related by

$$\beta = \sqrt{k_0^2 - \alpha^2}. \tag{65}$$

Thus $\tilde{\Gamma}(\alpha)$, the Fourier transform of the received field, is proportional to $\tilde{O}(\alpha,\beta - k_0)$, the Fourier transform of the object along a circular arc. This result has been called the Fourier Diffraction Projection Theorem [13] and is diagramed in Fig. 1.

We have derived an expression, Eq. (63), that relates the scattering by an object to the field received at a line. Within the diffraction limit it is possible to invert this relation to estimate the object scattering distribution based on the received field.

3. THE RECONSTRUCTION PROCESS

The best that can be hoped for in any tomographic experiment is to estimate the Fourier transform of the object for all frequencies within a disk centered at the origin. For objects that do not have any frequency content outside the disc, then the reconstruction procedure is perfect.

There are several different procedures that can be used to estimate the object function from the forward scattered fields. A single plane wave provides exact information (up to a frequency of $\sqrt{2}k_0$) about the Fourier transform of the object along a circular arc. Two of the simplest procedures involve changing the orientation and frequency of the incident plane waves to move the frequency domain arcs to a new position. By appropriately choosing an orientation and a frequency it is possible to estimate the Fourier transform of the object at any given frequency. In addition, it is possible to change the radius of the semicircular arc by varying the frequency of the incident field and thus generating an estimate of the entire Fourier transform of the object. This concept is contained in a companion paper by Farhat elsewhere in this volume.

An important point to notice here is that reflection and transmission tomography provide completely different information about the object (see Fig. 5). A transmission experiment gives information about the object up to a spatial frequency of $\sqrt{2}k_0$. On the other hand, a reflection experiment gives the information for spatial frequencies between

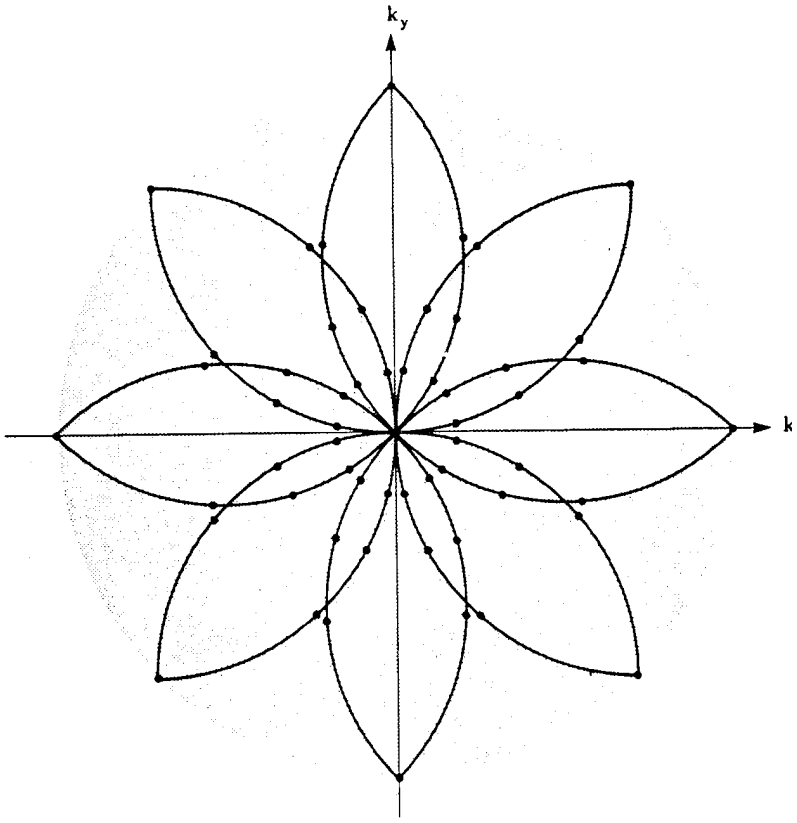

Fig. 7. Estimates of the object's two dimensional Fourier transform are available along the circular arcs for plane wave illumination.

$\sqrt{2}k_0$ and $2k_0$. In principle it should be possible to combine the two experiments and obtain an estimate of the amplitude of all the spatial frequencies up to $2k_0$.

3.1 Plane Wave Illumination

The most straightforward data collection procedure consists of rotating the object and measuring the scattered field for different orientations. Each orientation will produce an estimate of the object's Fourier transform along a circular arc and these arcs will rotate as the object is rotated. When the object is rotated through a full 360 degrees an estimate of the object will be available for the entire Fourier disk.

The coverage for this method is shown in Fig. 7 for a simple experiment with 8 projections of 9 samples each. Notice that there are two arcs that pass through each point of Fourier space. Generally it will be necessary to choose one estimate as better.

On the other hand, if the reflected data is collected by measuring the field on the same side of the object as the source then estimates of the object are available for frequencies greater than $\sqrt{2}k_0$. This follows from Fig. 5.

The first experimental results for diffraction tomography were presented by Carter and Ho [20], [21], [22]. They used an optical plane wave to illuminate a small glass object and were able to measure the scattered fields using a hologram. Later a group of researchers at the University of Minnesota carried out the same experiments using ultrasound and gelatine phantoms. Their results are discussed in Ref. [23].

3.2 Synthetic Aperture

Nahamoo and Kak [24], [25] and Devaney [26] have proposed a method that requires only two rotational views of an object. Consider an arbitrary source of waves in the transmitter plane as shown in Fig. 8. The transmitted field, ψ_t, can be represented as a weighted set of plane waves by taking the Fourier transform of the transmitter aperture function [27]. Doing this the transmitted field can be expressed as

$$\psi_t(x) = \frac{1}{4\pi^2}\int_{-\infty}^{\infty} A_t(k_x)e^{jk_x x}dk_x. \tag{66}$$

Moving the source to a new position, η, the plane wave decomposition of the transmitted field becomes

$$\psi_t(x;\eta) = \frac{1}{4\pi^2}\int_{-\infty}^{\infty} (A_t(k_x)e^{-jk_x\eta})e^{jk_x x}dk_x. \tag{67}$$

Given the plane wave decomposition, the incident field in the plane follows simply as

$$\psi_i(\eta;x,y) = \int_{-\infty}^{\infty}\left(\frac{1}{4\pi^2}A_t(k_x)e^{-jk_x\eta}\right)e^{j(k_x x+k_y y)}dk_x. \tag{68}$$

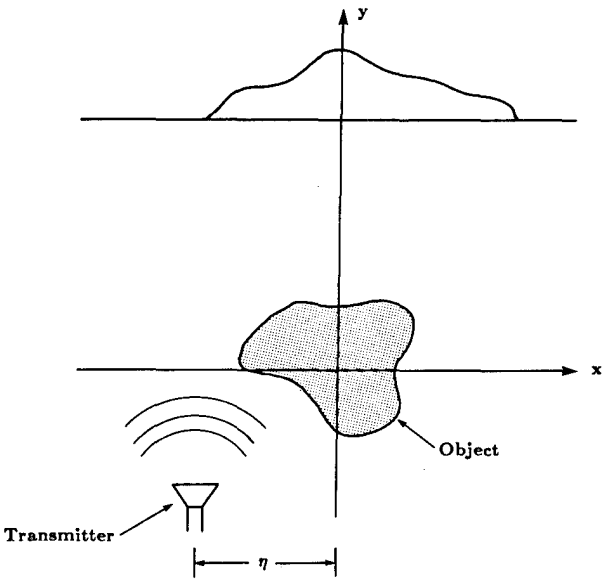

Fig. 8. A typical synthetic aperture tomography experiment.

Eq. (59) is an equation for the scattered field from a single plane wave. Because of the linearity of the Fourier transform, the effect of each plane wave, $e^{j(k_x x + k_y y)}$, can be weighted by the expression in brackets above and superimposed to find the Fourier transform of the total scattered field due to the incident field $\psi_t(x;\eta)$ as [24]

$$\tilde{\psi}_s(\eta,\alpha) = \int_{-\infty}^{\infty} (A_t(k_x)e^{-jk_x\eta}) \frac{O(\alpha - k_x, \gamma - k_y)}{j2\gamma} e^{j\gamma l_0} dk_x. \tag{69}$$

The quantity $\tilde{\psi}_s(\eta;\alpha)$ represents the one-dimensional Fourier transform of the field along a receiver line at a distance of l_0 from the origin due to a point source at η. Taking the Fourier transform of both sides with respect to the transmitter position, η, the Fourier transform of the scattered field with respect to both the transmitter and the receiver position is given by

$$\tilde{\psi}_s(k_x;\alpha) = A_t(k_x) \frac{O(\alpha - k_x, \gamma - k_y)}{j2\gamma} e^{j\gamma l_0}. \tag{70}$$

This approach is named synthetic aperture because a phase is added to the field measured for each transmitter position to synthesize a transmitted plane wave. Thus this method has much in common with the theory of phased arrays. Figure 9 shows that by properly phasing the wave transmitted at each transmitter location a plane wave can be generated that travels in an arbitrary direction. Since the system is linear it doesn't matter whether the phase is added to the transmitted signal or as part of the reconstruction procedure. Thus multiplying the received field for each transmitter position by the pure phase term $e^{-jk_x\eta}$, where η represents the location of the transmitter, is equivalent to an experiment with an incident plane wave with the direction vector $(k_x, \sqrt{k_0^2 - k_x^2})$. The concept is similar to that

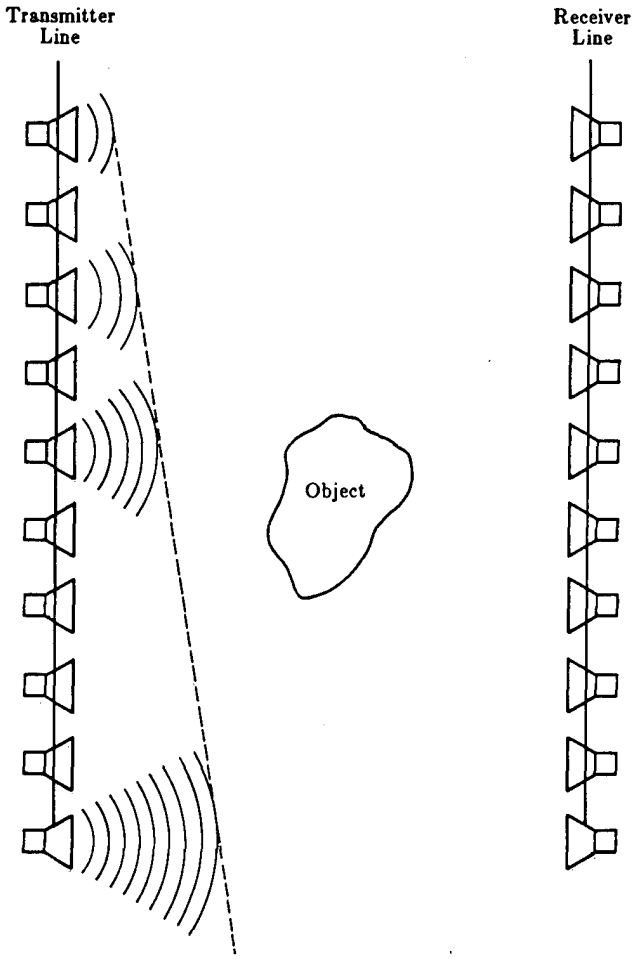

Fig. 9. By adding a phase to the field transmitted from each transmitter any desired plane wave can be synthesized.

of beam steering as discussed by Foti *et al* elsewhere in this volume.

By collecting the scattered field along the receiver line as a function of transmitter position, η, an expression can be written for the scattered field. Like the simpler case with plane wave incidence, the scattered field is related to the Fourier transform of the object along an arc. Unlike the previous case, though, the coverage due to a single view of the object is a pair of circular disks as shown in Fig. 10. Here a single view consists of transmitting from all positions in a line and measuring the scattered field at all positions along the receiver line. By rotating the object by 90 degrees it is possible to generate the complimentary pair of disks and to fill the Fourier domain out to $\pm 2k_0$ along both axes.

The coverage shown in Fig. 10 is constructed by calculating $(\vec{K} - \vec{\Lambda})$ for all vectors $(\vec{K})$ and $(\vec{\Lambda})$ that satisfy the experimental constraints. Not only must each vector satisfy the wave equation, but it is also necessary that only forward traveling plane waves be used. The dashed line in Fig. 10 shows the valid propagation vectors $(-\vec{\Lambda})$ for the transmitted waves. To each possible vector $(-\vec{\Lambda})$ a semicircular set of

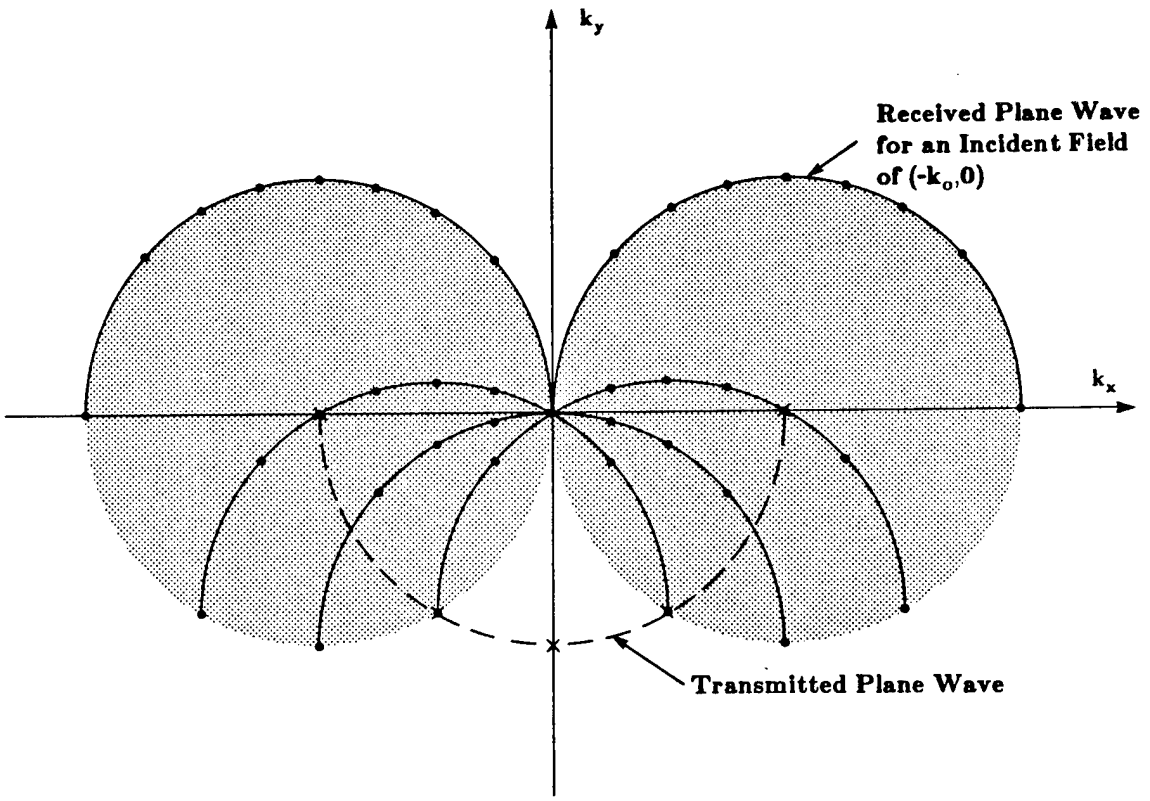

Fig. 10. Estimates of the Fourier transform of an object in a synthetic aperture experiment are available in the shaded region.

vectors representing each possible received wave can be added. The locus of received plane waves is shown as a solid semi-circle centered at each of the transmitted waves indicated by an "x." The entire coverage for the synthetic aperture approach is shown as the shaded areas.

In addition to the diffraction tomography configurations proposed by Mueller and Nahamoo other approaches have been proposed. In Vertical Seismic Profiling (VSP) [26] the scattering between the surface of the Earth and a borehole is measured. Alternately a broadband incident field can be used to illuminate the object. In both cases, the goal is to estimate the Fourier transform of the object.

In geophysical imaging it is not possible to generate or receive waves from all positions around the object. If it is possible to drill a borehole then it is possible to perform VSP and obtain information about most of the object. A typical experiment is shown in Fig. 11. So as to not damage the borehole, acoustic waves are generated at the surface using acoutic detonators or other methods and the scattered field is measured in the borehole.

The coverage in the frequency domain is similar to the synthetic aperture approach. Plane waves at an arbitrary downward direction are synthesized by appropriately phasing the transmitting transducers. The receivers will receive any waves traveling to the right. The resulting coverage for this method is shown in Fig. 12a. If it can be assumed that the object function is real valued then the symmetry of the Fourier transform for real valued functions can be used to obtain the coverage in Fig. 12b.

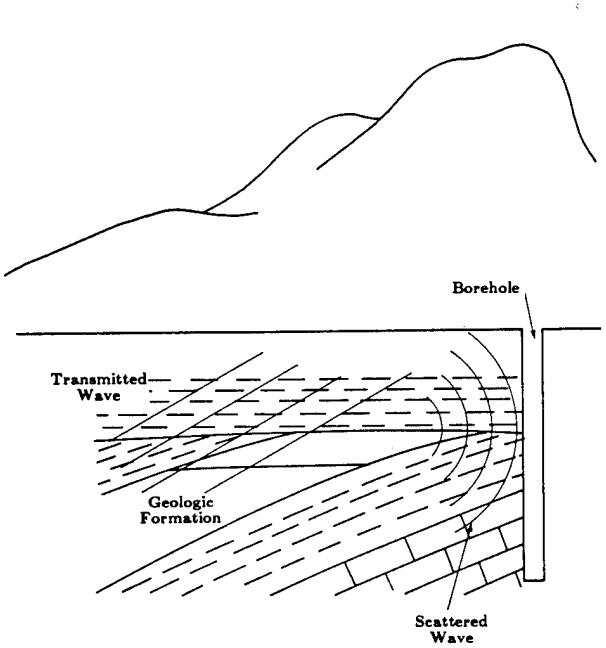

Fig. 11. A typical Verticla Seismic Profiling (VSP) experiment.

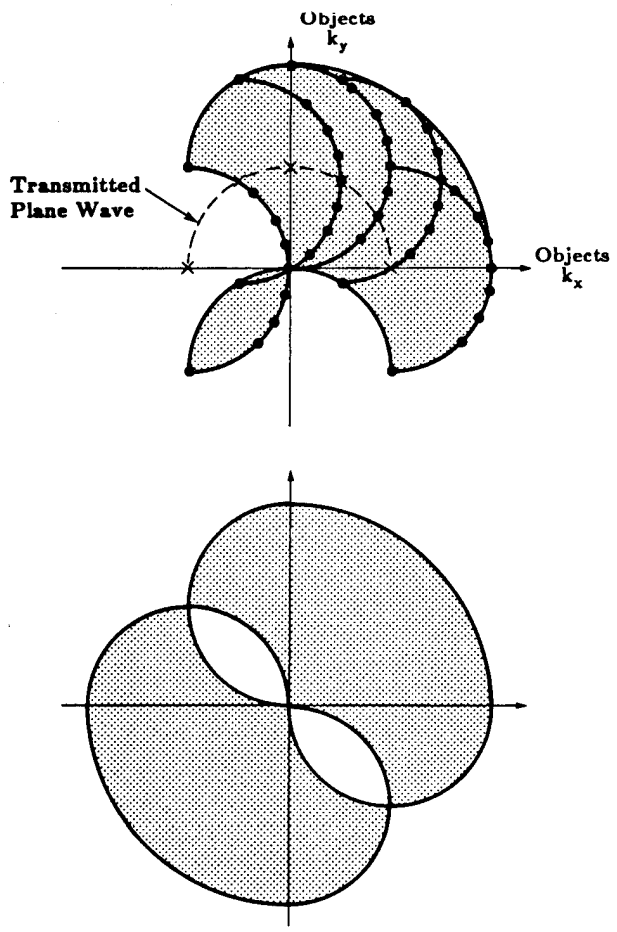

Fig. 12. Estimate of the Fourier transform of an object are available in the shaded region for a VSP experiment (a). If, in addition, the object is real valued then the symmetry of the Fourier transform can be used to get the coverage shown in (b).

3.3 Broadband Illumination

It is also possible to perform an experiment for broadband illumination [19]. Up until this point only narrow band illumination has been considered; wherein the field at each point can be completely described by its complex amplitude.

Now consider a transducer that illuminates an object with a wave of the form $a_t(k_x,t)$. Taking the Fourier transform in the time domain this wave can be decomposed into a number of experiments. Let

$$A_t(k_x,\omega) = \int_{-\infty}^{\infty} a_t(k_x,t)e^{-j\omega t}dt \tag{71}$$

where ω is related to k_ω by

$$k_\omega = \frac{c}{\omega}, \tag{72}$$

c is the speed of propagation in the media and the wavevector (k_x,k_y) satisfies the wave equation

$$k_x^2 + k_y^2 = k_\omega^2. \tag{73}$$

If a plane wave illumination of spatial frequency k_x and a temporal frequency ω leads to the scattered field $u_s(k_x,w;y)$, then the total scattered field is given by a weighted superposition of the scattered fields or

$$\Psi_s(k_x;y) = \int_{-\infty}^{\infty} A_t(k_x,\omega)u_s(k_x,\omega;y)d\omega. \tag{74}$$

For plane wave incidence, the coverage available with this method is shown in Fig. 13a. Figure 13b shows that by doing four experiments at 0, 90, 180, and 270 degrees it is possible to gather information about the entire object.

3.4 Reconstruction by Interpolation

The Fourier Diffraction Theorem as derived in Section 2 shows that when an object is illuminated with a plane wave

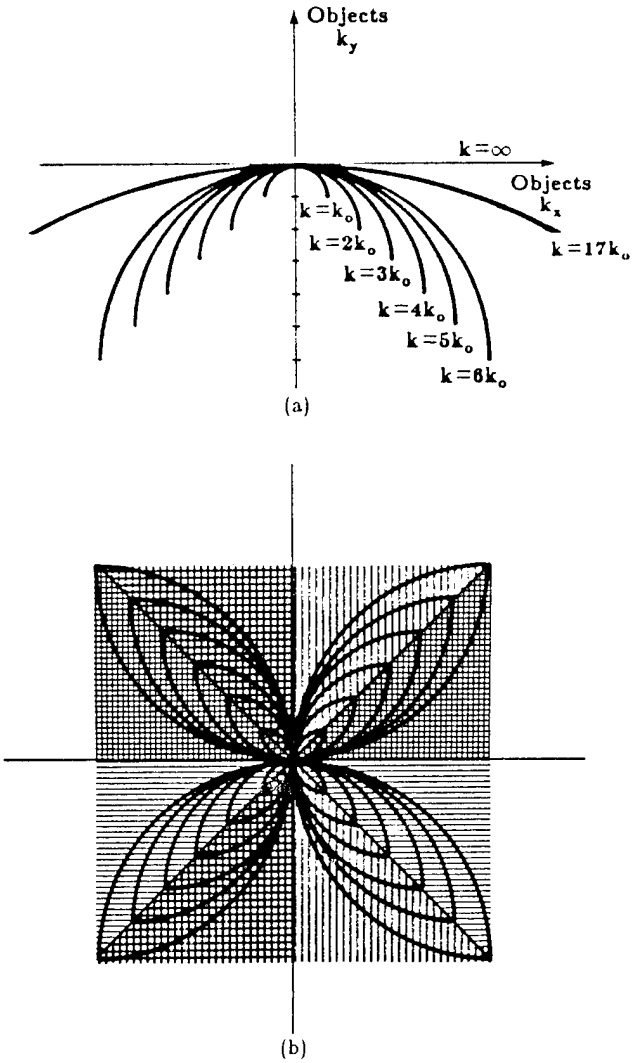

Fig. 13. One view of a broadband diffraction tomography experiment will generate estimates of the object along the arcs in (a). With four views of the object complete coverage can be obtained as shown in (b).

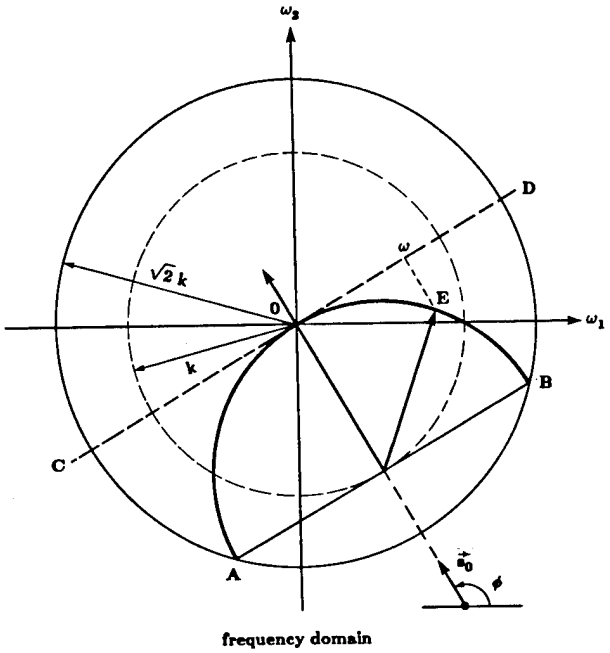

Fig. 14. Each projection is measured using the phi-omega coordinate system shown here.

traveling in the positive y-direction, the Fourier transform of the forward scattered fields gives values of the object's Fourier transform on an arc. Therefore, if an object is illuminated from many different directions it is possible, in principle, to fill up a disc of diameter $\sqrt{2}k_0$ in the frequency domain with samples of the Fourier transform of the object and then reconstruct the object by direct Fourier inversion. Therefore, diffraction tomography, using forward scattered data only, determines the object up to a maximum angular spatial frequency of $\sqrt{2}k_0$. To this extent, the reconstructed object is a low pass version of the original. In practice, the loss of resolution caused by this bandlimiting is negligible, being more influenced by considerations such as the aperture sizes of the transmitting and receiving elements, etc.

The fact that the frequency domain samples are available over circular arcs is a source of computational difficulty in reconstruction algorithms for diffraction tomography since for convenient display it is desired to have samples over a rectangular lattice. It should also be clear that by illuminating the object over 360°, a *double* coverage of the frequency domain is generated; note, however, that this double coverage is uniform. If the illumination is restricted to a portion of 360°, there still will be a complete coverage of the frequency domain; however, in that case, there would be patches in the (ω_1,ω_2)-plane where there would be a double coverage. In reconstructing from circular arc grids to rectangular grids, it is often easier to contend with a uniform double coverage, as opposed to a coverage that is single in most areas and double in patches.

However, for some applications not given to data collection from all possible directions, it is useful to bear in mind that it is not necessary to go completely around an object to get complete coverage of the frequency domain. In principle, it should be possible to get an equal quality reconstruction when illumination angles are restricted to a 180°-plus interval. The few angles in excess of 180° are required to complete the coverage of the frequency domain.

There are two computational strategies for reconstructing the object given measurements of the scattered field. As pointed out by [28] the two algorithms can be considered as interpolation in the frequency domain and in the space domain and are analogous to the direct Fourier inversion and backprojection algorithms of conventional tomography. Unlike conventional tomography, where backprojection is the preferred approach, the computational expense of space domain interpolation of diffracted projections makes frequency domain interpolation the preferred approach.

The remainder of this section will consist of derivations of the frequency domain interpolation algorithm. The reader is referred to Devaney [9] and Pan [13] for excellent explanations of the space domain interpolation algorithm and [29] for the general case.

In order to discuss the frequency domain interpolation between a circular grid on which the data is generated by diffraction tomography, and a rectangular grid suitable for image reconstruction, parameters for representing each grid must be selected. Then the relationship between the two sets of parameters can be written.

In Section 2, $\Psi_B(\omega)$ was used to denote the Fourier transform of the transmitted data when an object is illuminated with a plane wave traveling along the positive y direction. Now $\Psi_{B,\phi}(\omega)$ is used to denote this Fourier transform, where the subscript ϕ indicates the angle of illumination. This angle is measured as shown in Fig. 14. Similarly, $Q(\omega,\phi)$ will be used to indicate the values of $O(\omega_1,\omega_2)$ along a semi-circular arc oriented at an angle ϕ as shown in Fig. 15.

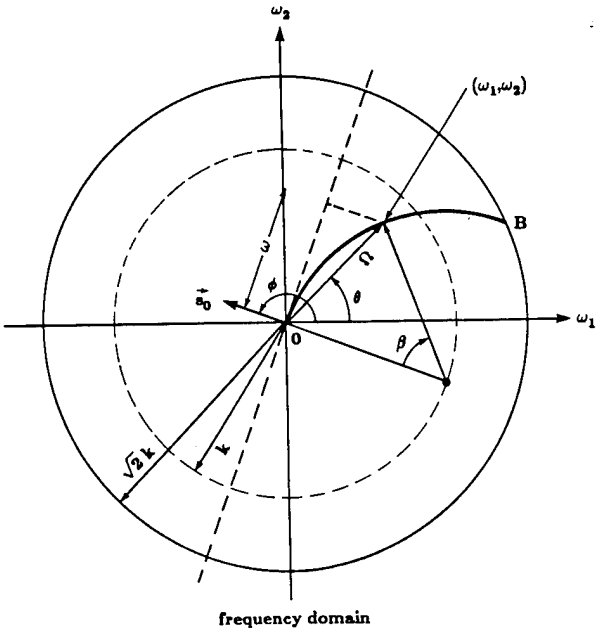

Fig. 15. A second change of variables is used to relate the projection data to the object's Fourier transform.

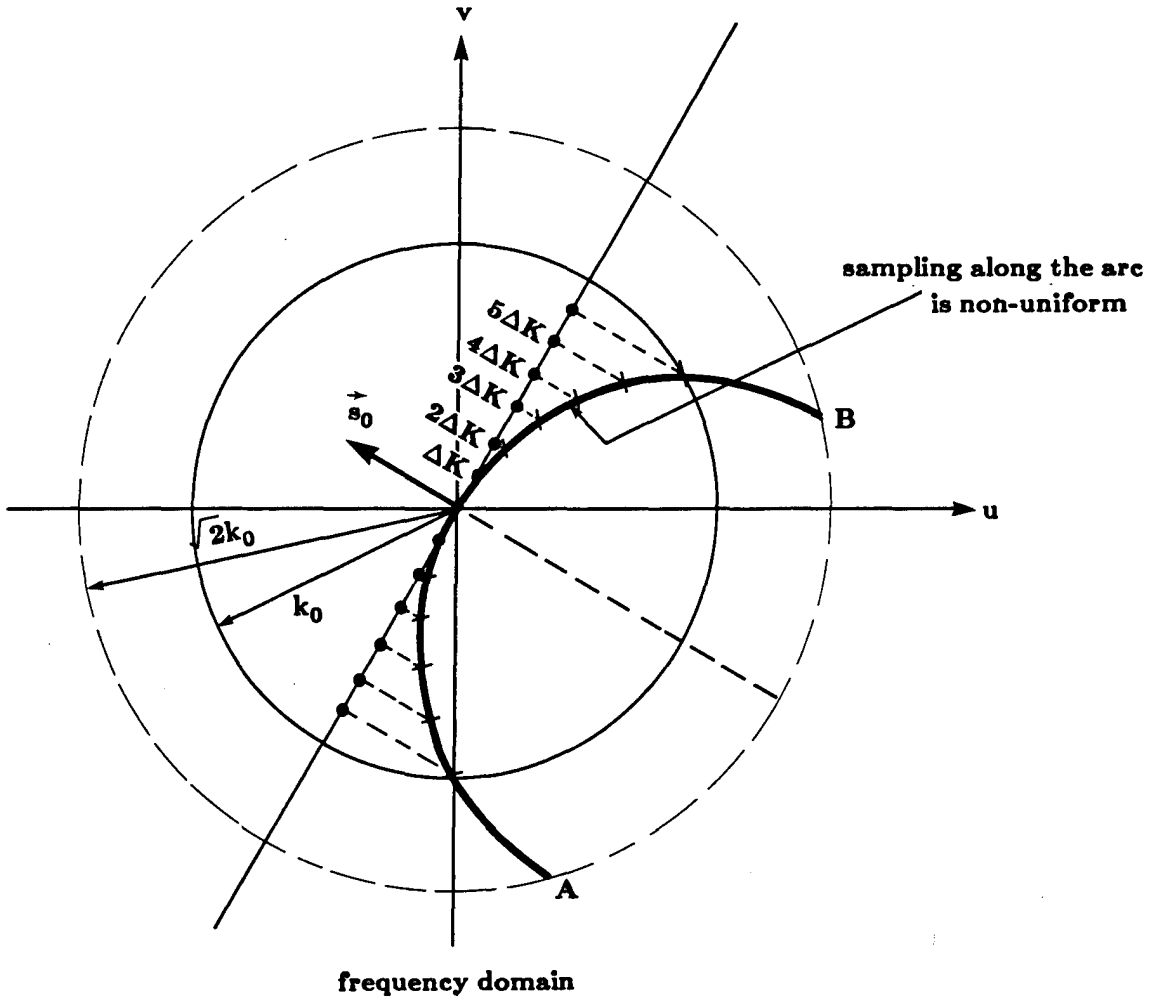

Fig. 16. Uniformly sampling the projection in the space domain leads to uneven spacing of the samples of the Fourier transform of the object along the semi-circular arc.

Therefore, when an illuminating plane wave is incident at angle ϕ, the equality

$$\Psi_B(\omega,l_0) = \frac{j}{2\sqrt{k_0^2-\omega^2}} e^{j\sqrt{k_0^2-\omega^2}l_0} O(\omega, \sqrt{k_0^2-\omega^2} - k_0) \tag{75}$$

can be rewritten as

$$\Psi_{B,\phi}(\omega) = \frac{j}{2}\frac{1}{\sqrt{k_0^2-\omega^2}} \exp[jl_0\sqrt{k_0^2-\omega^2}]Q(\omega,\phi)$$
$$\text{for } |\omega| < k_0. \tag{76}$$

In most cases, the transmitted data will be uniformly sampled in space, and a *discrete* Fourier transform of this data will generate uniformly spaced samples of $\Psi_{B,\phi}(\omega)$ in the ω domain. Since $Q(\omega,\phi)$ is the Fourier transform of the object along the circular arc AOB in Fig. 14, and since κ is the projection of a point on the circular arc onto the tangent line CD, the uniform samples Q in λ translate into non-uniform samples along the arc AOB as shown in Fig. 16. For this reason, designate each point on the arc AOB by its (ω,ϕ) parameters. [Note that (ω,ϕ) are *not* the polar coordinates of a point on arc AOB in Fig. 15. Therefore, ω is *not* the radial distance in the (ω_1,ω_2) plane. For point E shown, the parameter ω is obtained by projecting E onto line CD.] The rectangular coordinates in the frequency domain will remain (ω_1,ω_2).

Before the relationships between (ω,ϕ) and (ω_1,ω_2), are presented, it must be mentioned that the points generated by the AO and OB portions of the arc AOB must be considered separately as ϕ is varied from 0 to 2π. This is done because, as mentioned before, the arc AOB generates a double coverage of the frequency domain, as ϕ is varied from 0 to 2π, which is undesirable for discussing a one-to-one transformation between the (ω,ϕ) parameters and the (ω_1,ω_2) coordinates.

Now reserve (ω,ϕ) parameters to denote the arc grid generated by one projection. It is important to note that for this arc grid, ω varies from 0 to k and ϕ from 0 to 2π.

The transformation equations between (ω,ϕ) and (ω_1,ω_2)

will now be presented. This is accomplished in a slightly round-about manner by first defining polar coordinates (Ω,θ) in the (ω_1,ω_2)-plane as shown in Fig. 15. In order to go from (ω_1,ω_2) to (ω,ϕ), first transform from the former coordinates to (Ω,θ) and then from (Ω,θ) to (ω,ϕ). The rectangular coordinates (ω_1,ω_2) are related to the polar coordinates (Ω,θ) by (Fig. 15)

$$\Omega = \sqrt{\omega_1^2 + \omega_2^2} \tag{77}$$

$$\theta = \tan^{-1}\left(\frac{\omega_2}{\omega_1}\right). \tag{78}$$

In order to relate (Ω,θ) to (ω,ϕ), a new angle β, which is the angular position of a point (ω_1,ω_2) on arc OB in Fig. 15, is introduced. Note from the figure that the point characterized by angle β is also characterized by parameter ω. The relationship between ω and β is given by

$$\omega = k_0 \sin\beta. \tag{77}$$

The following relationship exists between the polar coordinates (Ω,θ) on the one hand and the parameters β and ϕ on the other:

$$\beta = 2\sin^{-1}\frac{\Omega}{2k_0} \tag{79}$$

$$\phi = \theta + \frac{\pi}{2} + \frac{\beta}{2}. \tag{80}$$

By substituting Eq. (79) in (77) and then using (77), ω can be expressed in terms of ω_1 and ω_2. This result is shown below. Similarly, by substituting Eq. (78) in (80), the following expression is obtained for ω and ϕ

$$\omega = \sin\left\{2\sin^{-1}\left(\frac{\sqrt{\omega_1^2 + \omega_2^2}}{2k_0}\right)\right\} \tag{81}$$

$$\theta = \tan^{-1}\left(\frac{\omega_2}{\omega_1}\right) + \sin^{-1}\left(\frac{\sqrt{\omega_1^2 + \omega_2^2}}{2k_0}\right) + \frac{\pi}{2}. \tag{82}$$

These are the transformation equations for interpolating from the (ω,ϕ) parameters used for data representation to the (ω_1,ω_2) parameters needed for inverse transformation.

To convert a particular rectangular point into (ω,ϕ) domain, substitute its ω_1 and ω_2 values in Eqs. (81) and (82). The resulting values for ω and ϕ may not correspond to any for which $Q(\omega,\phi)$ is known. By virtue of Eq. (76), $Q(\omega,\phi)$ will only be known over a uniformly sampled set of values for ω and ϕ. In order to determine Q at the calculated ω and ϕ, the following procedure is used. Given $N_\omega \times N_\phi$ uniformly located samples, $Q(\omega_i,\phi_j)$, calculate a bilinearly interpolated value of this function at the desired ω and ϕ by using

$$Q(\omega,\phi) = \sum_{i=1}^{N_\omega}\sum_{j=1}^{N_\phi} Q(\omega_i,\phi_j)h_1(\omega - \omega_i)h_2(\phi - \phi_j), \tag{83}$$

where

$$h_1(\omega) = \begin{cases} 1 - \dfrac{|\omega|}{\Delta\omega} & 0 \\ |\omega| \le \Delta\omega & \text{otherwise,} \end{cases} \tag{84}$$

and

$$h_2(\phi) = \begin{cases} 1 - \dfrac{|\phi|}{\Delta\phi} & 0 \\ |\phi| \le \Delta\phi & \text{otherwise;} \end{cases} \tag{85}$$

$\Delta\phi$ and $\Delta\omega$ are the sampling intervals for ϕ and ω, respectively. When expressed in the manner shown above, bilinear interpolation may be interpreted as the output of a filter whose impulse reponse is $h_1(\omega)h_2(\phi)$.

The results obtained with bilinear interpolation can be considerably improved if the sampling density in the (ω,ϕ)-plane is increased by using the computationally efficient method of zero-extending the inverse two-dimensional inverse *Fast Fourier Transform* (FFT) of the $Q(\omega_i,\phi_j)$ matrix. The technique consists of first taking a two-dimensional inverse FFT of the $N_\omega \times N_\phi$ matrix consisting of the $Q(\omega_i,\phi_j)$ values, zero-extending the resulting $N_\omega \times N_\phi$ array of numbers to, perhaps, $mN_\omega \times nM_\phi$ and then taking the FFT of this new array. The result is an mn-fold increase in the density of samples in the (ω,ϕ)-plane. After computing $Q(\omega,\phi)$ at each point of a rectangular grid by the procedure outlined above, the object f(x,y) is obtained by a simple 2-D inverse FFT.

The use of bilinear interpolation and zero padding are both good techniques for resampling a function but they are used here in a non-standard way. Typically interpolation algorithms are derived assuming that the sampled data can be described as nearly linear (when using bilinear interpolation) and frequency limited (when using Fourier domain zero padding) [30], [31], [32]. In this application, when resampling the data from a circular grid to a rectangular grid, the function is assumed to be smooth in the Fourier domain. This assumption is reasonable since the data is assumed to be well behaved.

The interpolation described above, however, is carried out in a rectilinear version of the (ω,ϕ) coordinate system. Thus four points in the (ω,ϕ) space, where data is available, are first assumed to be at the four corners of a rectangle and then the interpolation is calculated for a point in the middle. This is an approximation because the four data points actually define a smooth function that is defined along four points on two circular arcs. As will be seen in the reconstructions, the effect of this approximation is small; but it should be remembered when comparing interpolation schemes.

4. LIMITS OF FIRST ORDER APPROXIMATIONS

In diffraction tomography there are different approximations involved in the forward and inverse directions. In the forward process it is necessary to assume that the object is weakly scattering so that either the Born or the Rytov approximations can be used. Once we arrive at an expression for the scattered field it is necessary to not only measure the scattered fields but then to numerically implement the inversion process.

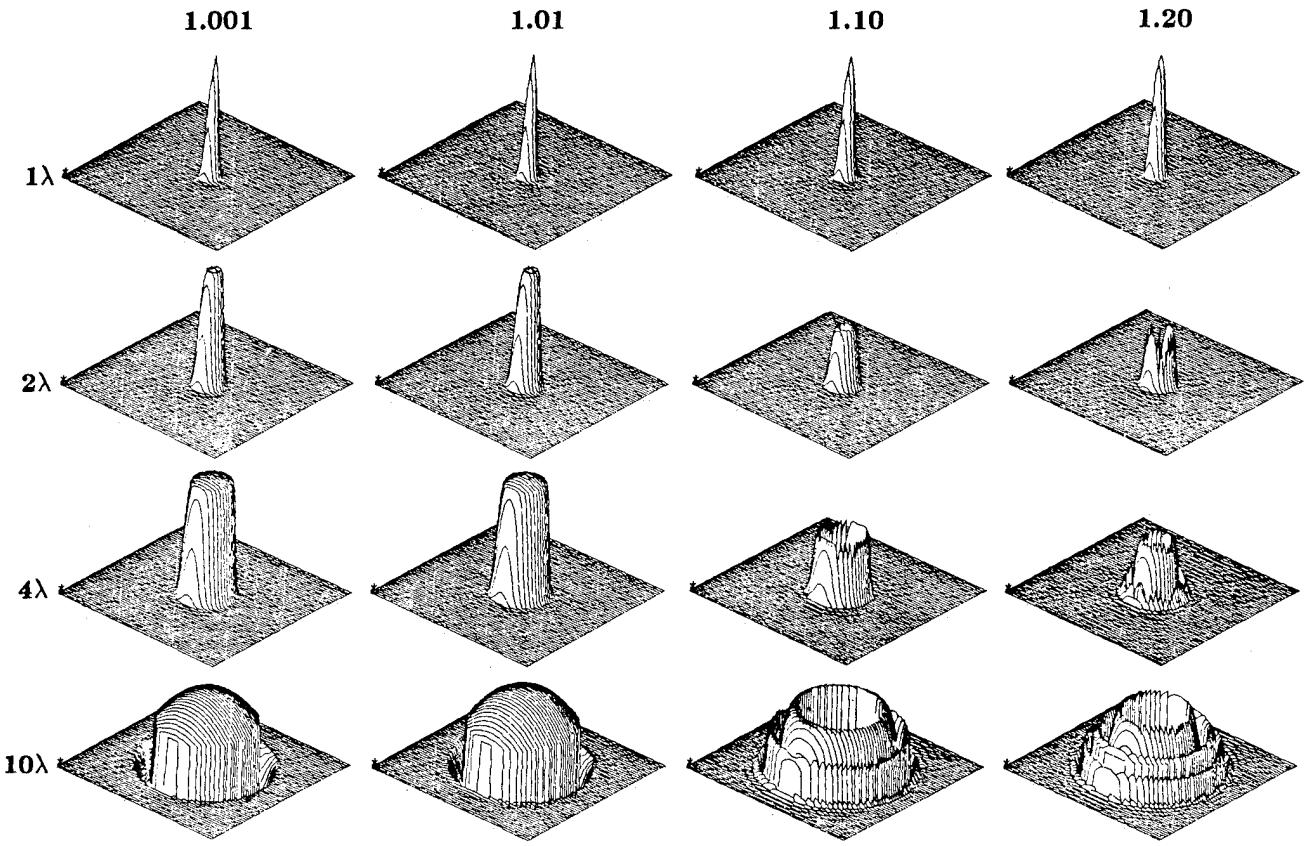

Fig. 17. Simulated reconstructions using the Born approximation for 16 objects with four refractive indices between 1.001 and 1.20 and four radii between 1 and 10λ.

The mathematical and experimental effects limit the reconstruction in different ways. The most severe mathematical limitations are imposed by the Born and the Rytov approximations. These approximations are fundamental to the reconstruction process and limit the range of objects that can be examined. On the other hand, the experimental limitations are caused because it is only possible to collect a finite amount of data. Up to the limit in resolution caused by evanescent waves, it is possible to improve a reconstruction by collecting more data.

By carefully setting up the simulations it is possible to separate the effects of these errors. To study the effects of the Born and Rytov approximations, it is necessary to calculate (or even measure) the exact fields and them make use of the best possible (most exact) reconstruction formulas available. The difference between the reconstruction and the actual object can then be used as a measure of the quality of the approximations.

Only the mathematical limitations will be described here. For a discussion of some of the experimental factors the reader is referred to [33], [34].

4.1 Qualitative Analysis

The exact field for the scattered field from a cylinder as shown by Weeks [35] was calculated for cylinders of various sizes and refractive index. In the simulations that follow a single plane wave was incident on the cylinder and the scattered field was calculated along a line at a distance of 100 wavelengths from the origin.

At the receiver line the received wave was measured at 512 points spaced at 1/2 wavelength intervals. In all cases the rotational symmetry of a single cylinder at the origin was used to reduce the computation time of the simulations.

The simulations were performed for refractive indices that ranged from 0.1% change (refractive index of 1.001) to a 20% change (refractive index of 1.2). For each refractive index, cylinders of size 1, 2, 4, and 10 wavelengths were reconstructed. This gave a range of phase changes across the cylinder [see Eq. (23) above] from 0.004π to 8π. The resulting reconstructions using the Born approximation are shown in Fig. 17.

Clearly, all the cylinders of refractive index 1.001 in Fig. 17 were perfectly reconstructed. As Eq. (24) predicts, the results get worse as the product of refractive index and radius gets larger. The largest refractive index that was successfully reconstructed was for the cylinder in Fig. 17 of radius 1 wavelength and a refractive index that differed by 20% from the surrounding medium.

While it is hard to evaluate the two dimensional reconstructions, it is certainly reasonable to conclude that only cylinders where the phase change across the object was less

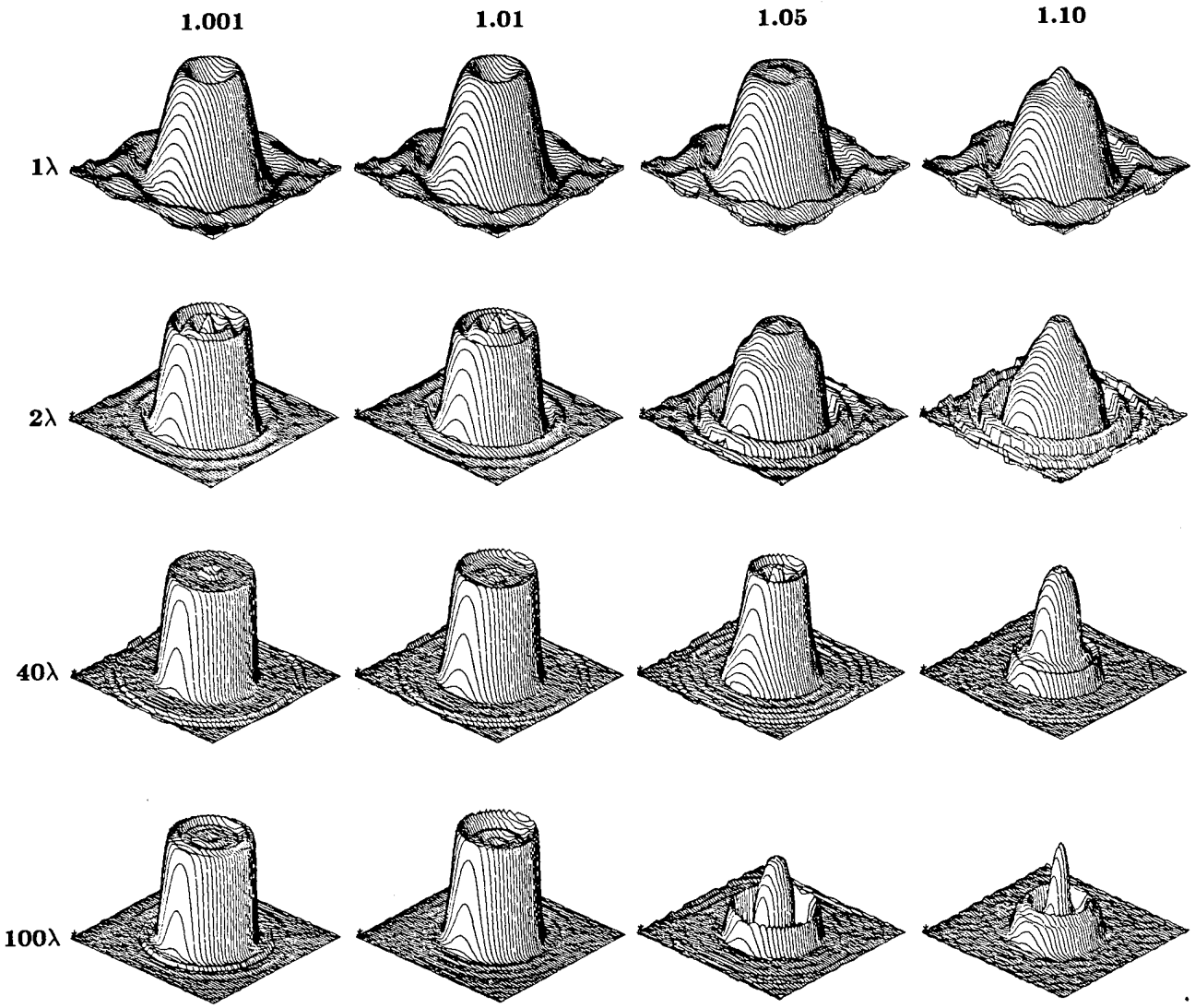

Fig. 18. Simulated reconstructions using the Born approximation for 16 objects with four refractive indices between 1.001 and 1.10 and four radii between 1 and 100λ.

than or equal to 0.8π were adequately reconstructed. In general, the reconstruction for each cylinder where the phase change across the cylinder was greater than π shows severe artifacts near the center. This limitation in the phase change across the cylinder is consistent with the condition expressed in Eq. (24) above.

A similar set of simulations was also done for the Rytov approximation and is shown in Fig. 18. In this case the reconstructions were performed for cylinders of radius 1, 2, 40, and 100 λ and refractive indices of 1.001, 1.01, 1.05, and 1.10. Because of the large variation in cylinder sizes all reconstructions were performed so the estimated object filled half of the reconstruction matrix. While the error in the reconstructions does increase for larger cylinders and higher refractive indices, it is possible to successfully reconstruct larger objects with the Rytov approximation.

4.2 Qualitative Comparison of the Born and Rytov Approximation

Reconstructions using exact scattered data show the similarity of the Born and Rytov approximations for small objects with small changes in the refractive index. For a cylinder of radius 1 wavelength and a refractive index that differs by 1% from the surrounding medium, the resulting reconstructions are shown in Fig. 19. In both cases, the reconstructions are clean and the magnitude of the reconstructed change in refractive index is close to the simulated object.

On the other hand, the reconstructions of objects that are large or have a refractive index that differ by a factor of ca. 20% from unity, illustrate the differences between the Born and the Rytov approximations. Figure 20 shows a simulated

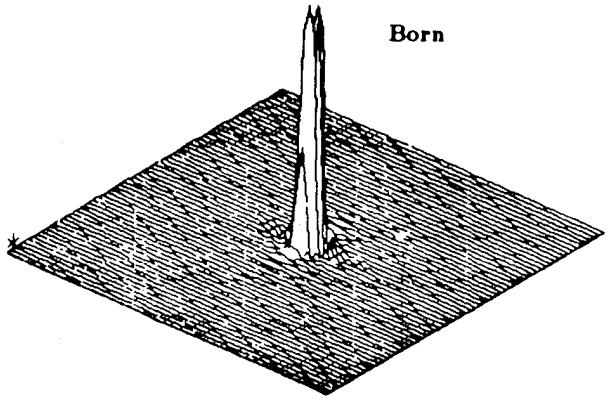

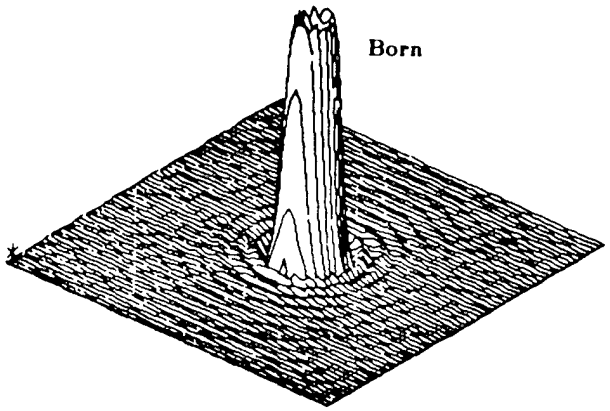

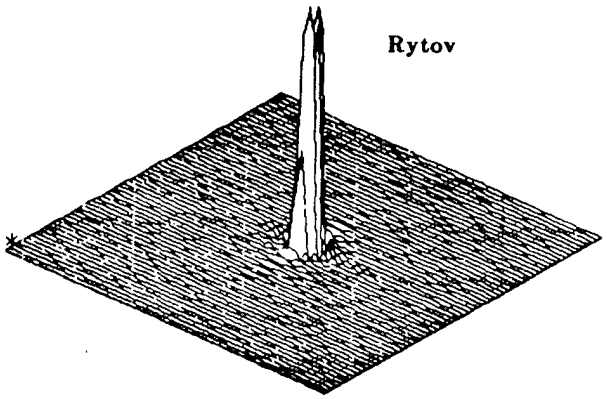

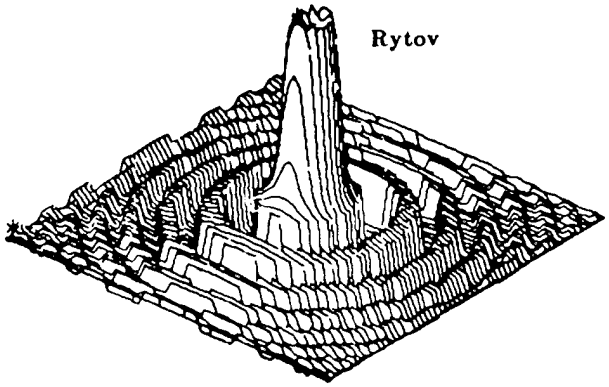

Fig. 19. Born and Rytov reconstructions of a cylinder of radius 1λ and 1.01 refractive index.

Fig. 20. Reconstructions of a cylinder of radius 1λ and refractive index 1.20 showing the advantage of the Born over the Rytov.

reconstruction for an object of radius 1 and refractive index 1.20. In this region the Born approximation is superior to the Rytov.

According to Chernov [17] and Keller [18] the Rytov approximation should be much superior to the Born for objects much larger than a wavelength. Reconstructions were done based on the exact scattered wave from a cylinder of radius 40 wavelengths and a refractive index that differed by 1% from the surrounding medium. The reconstructed refractive index is shown in Fig. 21. While the Born approximation has provided a good estimate of the size of the object, the reconstruction near the center is clearly not accurate.

The results in Figs. 20 and 21 are consistent with the regions of validity of the Born and Rytov approximations. The Born approximation is sensitive to the total phase shift in the object. Thus, in the reconstruction of Fig. 21 the Born approximation has done a good job of representing the step change in refractive index; but as the incident field undergoes a phase shift through the object, the reconstruction becomes poor. On the other hand, the Rytov approximation is sensitive to the change in refractive index. Thus the Rytov reconstruction is accurate near the center of the object but provides a very poor reconstruction near the boundary of the object.

4.3 Quantitative Studies

In addition to the qualitative studies, a quantitative study of the error in the Born and Rytov reconstructions was also performed. As a measure of error we used the relative mean squared error in the reconstruction of the object function integrated over the entire plane. If the actual object function is $O(\tilde{r})$ and the reconstructed object function is $O'(\tilde{r})$ then the relative Mean Squared Error (MSE) is

$$\text{MSE} = \frac{\iint [O(\tilde{r}) - O'(\tilde{r})]^2 d\tilde{r}}{\iint [O(\tilde{r})]^2 d\tilde{r}}. \tag{86}$$

To study the quantitative difference between the Born and the Rytov approximations, several hundred simulated reconstructions were performed. For each simulation the exact scattered field was calculated for a single cylinder with

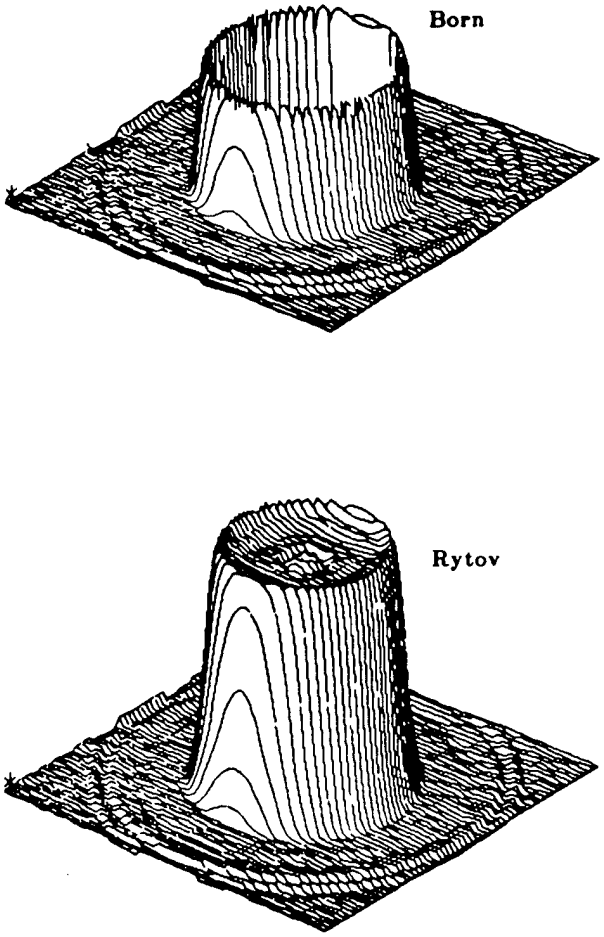

Fig. 21. Reconstructions of a cylinder of radius 40λ and refractive index 1.01 showing the advantage of the Rytov over the Born.

an arbitrary radius and refractive index. The reconstructions were divided into two sets to highlight the difference between the Born and the Rytov approximations.

The plots of Fig. 22 present a summary of the mean squared error for cylinders of 1, 2, and 3λ in radius and twenty refractive indices between 1.01 and 1.20. In each case the error for the Born approximation is shown as a solid line while the error for the Rytov approximation is shown as a dashed line. The exact scattered fields were calculated at 512 receiver points along a receiver line 10λ from the center of the cylinder.

Only for the 1λ cylinders is the relative mean squared error for the Born approximation always lower than the Rytov. It is interesting to note that while the Rytov approximation shows a steadily increasing error with higher refractive indices the error in the Born reconstruction is relatively constant until a threshold is reached. For the 2λ and the 3λ cylinder, this breakpoint occurs at a phase shift of 0.6 and 0.7π. Thus a criteria for the validity of the Born approximation is that the product of the radius of the cylinder in wavelengths and the change in refractive index must be less than 0.175.

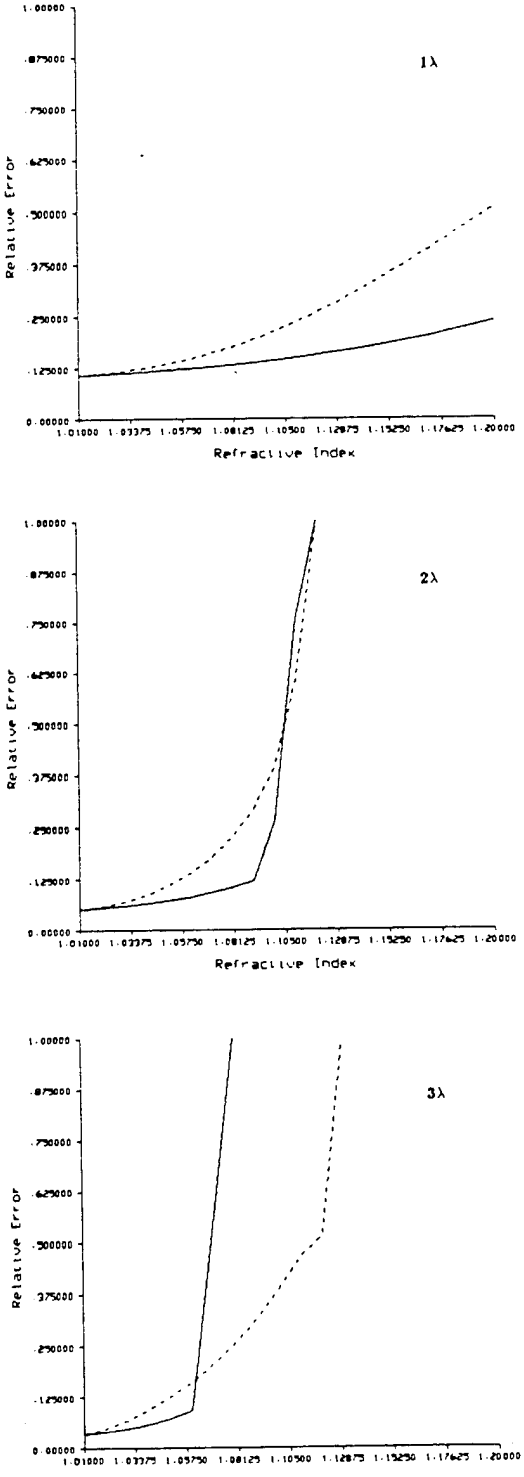

Fig. 22. The relative mean squared error for reconstructions using the Born (solid line) and Rytov (dashed line) approximations. The error for a total of 60 objects with a radius of 1, 2 and 3 wavelengths are shown.

Figure 23 presents a summary of the relative mean squared errors for cylinders of refractive index 1.01, 1.02, and 1.03 and for forty radii between 1 and 40λ. Because the size

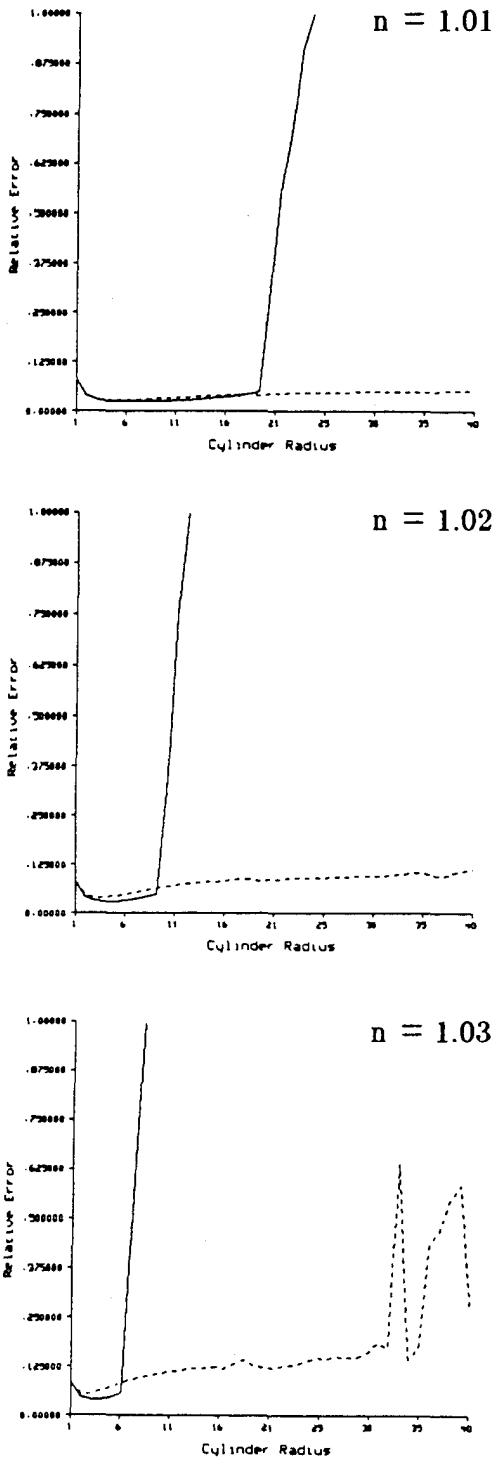

Fig. 23. The relative mean squared error for reconstructions using the Born (solid line) and Rytov (dashed line) approximations. The error for a total of 120 objects with a refractive index of 1.01, 1.02 and 1.03 are shown.

of the cylinders varied by a factor of forty, the simulation parameters were adjusted accordingly. For a cylinder of radius R the scattered field was calculated for 512 receivers along a line 2R from the center of the cylinder and spaced at 1/16R intervals.

In each of the simulations the Born approximation is only slightly better than the Rytov approximation until the Born approximation crosses its threshold with a phase shift of 0.7π. Because the error in the Rytov approximation is relatively flat it is clearly superior for large object and small refractive indices. Using simulated data and the Rytov approximation we have successfully reconstructed objects as large as 2000λ in radius.

4.4 Multiple Scattering Effects

The simulations above have only considered reconstructions of simple cylindrical objects with a constant refractive index. While these objects do have the advantage that it is possible to write an expression for the scattered fields they perhaps are not a good model of the real world. Simulations of more complicated objects are needed, but the calculation of the scattered fields are either more difficult or not possible at all. One type of object that can be modeled are those that consist of multiple cylinders.

A major source of difficulty with multi-component* objects is dealing with the interaction between the various components. Depending on the interaction between the components, the total scattered field may or may not bear any resemblance with the simple sum of the scattered fields for each of the components, assuming the others to be absent. A new computational procedure for calculating the inter-component interaction was presented in [36]. With the computer programs developed we are able to generate the scattered fields that are not limited by the first order assumption. Although the results shown will only include the second order fields for a multicomponent object, the computational procedure can easily be generalized for higher order scattering effects.

Since all currently available diffraction tomography algorithms are based on the assumption that the object satisfies the first order scattering assumption, it is interesting to test them under conditions when this assumption is violated. We have used the scattered fields obtained with the new computational procedure to test these algorithms, and shown the resulting artifacts. *Our main conclusion drawn from computer simulation study is that even when object inhomogeneities are as small as 5 percent of the background, multiple scattering can introduce severe distortion in reconstructions of multi-component objects.*

One can, in principle, obtain the exact solution to the wave equation for a multi-component object provided one is able to solve the boundary value problem for the entire object. In practice it is not possible to do so even for two- or three-

* By a single component object, we mean one that is composed of a single circular or elliptical cylinder. Analytical expressions are available for the scattered fields of such objects. A multiple-component object has more than one cylinder; for our purposes the cylinders will all be parallel to each other.

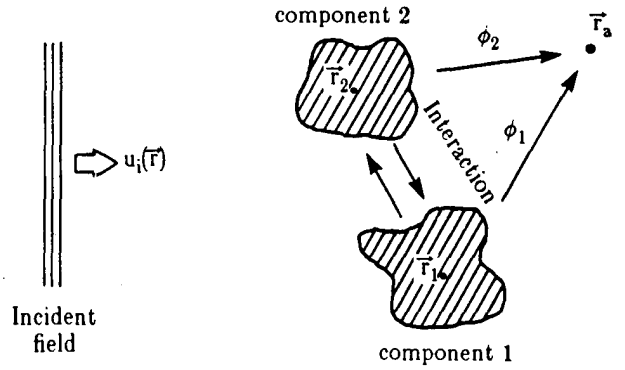

Fig. 24. A two component phantom illuminated with incident field $u_i(r)$.

component objects, and one must take recourse to computational procedures. We have based our algorithms on Twersky's theory in which the scattered field is expressed as an infinite summation of different order terms [15]. First order fields are obtained by considering the interaction of the original incident field with each component, assuming the others to be absent. First order fields caused by a component when incident on the other components generate the second order fields, and so on.

The basic elements of multiple scattering theory that we will use in our computational modeling will now be explained in detail with the help of a two component object (The approach is easily generalized to more than two components.) Figure 24 shows a two component phantom being illuminated by a field denoted by $u_i(\vec{r})$ (In the absence of the phantom the field everywhere will be $u_i(\vec{r})$.) We will use $u(\vec{r}_a)$ to denote the actual field at a point $(\vec{r}_a)$ as shown in the figure. $u(\vec{r}_a)$ is equal to

$$u(\vec{r}_a) = u_i(\vec{r}_a) + \phi_1(\vec{r}_a) + \phi_2(\vec{r}_a), \tag{87}$$

where $\phi_1(\vec{r}_a)$ and $\phi_2(\vec{r}_a)$ are, respectively, the scattered fields at $\vec{r}_a$ caused by the phantom components 1 and 2.

Let $u_{inc}(\vec{r}_i)$ be the incident field at the center of the i^{th} component, and let $o_s(\vec{r}_a,\vec{r}_i)$ be an operator function such that when it is applied to the fields incident on the scattering component at $\vec{r}_i$, it generates the scattered field at the observation point $\vec{r}_a$. In terms of o_s's, ϕ_1 and ϕ_2 are given by

$$\phi_i(\vec{r}_a) = o_s(\vec{r}_a,\vec{r}_i)u_{inc}(\vec{r}_i) \quad i = 1,2. \tag{88}$$

Substituting (88) in (87), we get

$$u(\vec{r}_a) = u(\vec{r}_a) + o_s(\vec{r}_a|\vec{r}_1)u_{inc}(\vec{r}_1) + o_s(\vec{r}_a|\vec{r}_2)u_{inc}(\vec{r}_2). \tag{89}$$

The field incident at the site of each scatterer may be expressed as

$$u_{inc}(\vec{r}_1) = u_i(\vec{r}_1) + o_s(\vec{r}_1|\vec{r}_2)u_{inc}(\vec{r}_2), \tag{90}$$

$$u_{inc}(\vec{r}_2) = u_i(\vec{r}_2) + o_s(\vec{r}_2|\vec{r}_1)u_{inc}(\vec{r}_1). \tag{91}$$

Substituting (90) and (91) in (89), we get

$$\begin{aligned} u(\vec{r}_a) = {} & u_i(\vec{r}_a) + o_s(\vec{r}_a|\vec{r}_1)u_i(\vec{r}_1) \\ & + o_s(\vec{r}_a|\vec{r}_2)u_i(\vec{r}_2) + o_s(\vec{r}_a|\vec{r}_1)o_s(\vec{r}_1|\vec{r}_2)u_{inc}(\vec{r}_2) \\ & + o_s(\vec{r}_a|\vec{r}_2)o_s(\vec{r}_2|\vec{r}_1)u_{inc}(\vec{r}_1). \end{aligned} \tag{92}$$

If we again substitute (90) and (91) in (92), we have the following expression

$$\begin{aligned} u(\vec{r}_a) = {} & u_i(\vec{r}_a) + o_s(\vec{r}_a|\vec{r}_1)u_i(\vec{r}_1) + o_s(\vec{r}_a|\vec{r}_2)u_i(\vec{r}_2) \\ & + o_s(\vec{r}_a|\vec{r}_1)o_s(\vec{r}_1|\vec{r}_2)u_i(\vec{r}_2) + o_s(\vec{r}_a|\vec{r}_2)o_s(\vec{r}_2|\vec{r}_1)u_i(\vec{r}_1) \\ & + o_s(\vec{r}_a|\vec{r}_1)o_s(\vec{r}_1|\vec{r}_2)o_s(\vec{r}_2|\vec{r}_1)u_{inc}(\vec{r}_1) \\ & + o_s(\vec{r}_a|\vec{r}_2)o_s(\vec{r}_2|\vec{r}_1)o_s(\vec{r}_1|\vec{r}_2)u_{inc}(\vec{r}_2). \end{aligned} \tag{93}$$

A more compact way to express the above equation is

$$\begin{aligned} u(\vec{r}_a) = {} & u_i(\vec{r}_a) + u_{\text{first-order}}(\vec{r}_a) + u_{\text{second-order}}(\vec{r}_a) \\ & + u_{\text{higher-order}}(\vec{r}_a). \end{aligned} \tag{94}$$

The quantities $u_{\text{first-order}}$, $u_{\text{second-order}}$ and $u_{\text{higher-order}}$ represent the first order, second order, and higher order contributions at the observation point $\vec{r}_a$. These are given by

$$u_{\text{first-order}}(\vec{r}_a) = o_s(\vec{r}_a|\vec{r}_1)u_i(\vec{r}_1) + o_s(\vec{r}_a|\vec{r}_2)u_i(\vec{r}_2) \tag{95}$$

$$\begin{aligned} u_{\text{second-order}}(\vec{r}_a) = {} & o_s(\vec{r}_a|\vec{r}_2)o_s(\vec{r}_2|\vec{r}_1)u_i(\vec{r}_1) \\ & + o_s(\vec{r}_a|\vec{r}_1)o_s(\vec{r}_1|\vec{r}_2)u_i(\vec{r}_2) \end{aligned} \tag{96}$$

$$\begin{aligned} u_{\text{higher-order}}(\vec{r}_a) = {} & o_s(\vec{r}_a|\vec{r}_1)o_s(\vec{r}_1|\vec{r}_2)o_s(\vec{r}_2|\vec{r}_1)u_{inc}(\vec{r}_1) \\ & + o_s(\vec{r}_a|\vec{r}_2)o_s(\vec{r}_2|\vec{r}_1)o_s(\vec{r}_1|\vec{r}_2)u_{inc}(\vec{r}_2) \end{aligned} \tag{97}$$

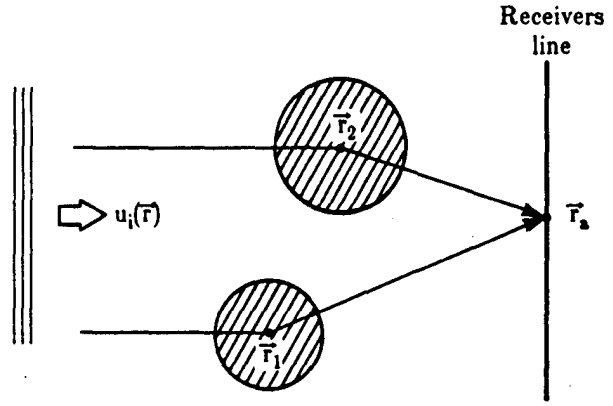

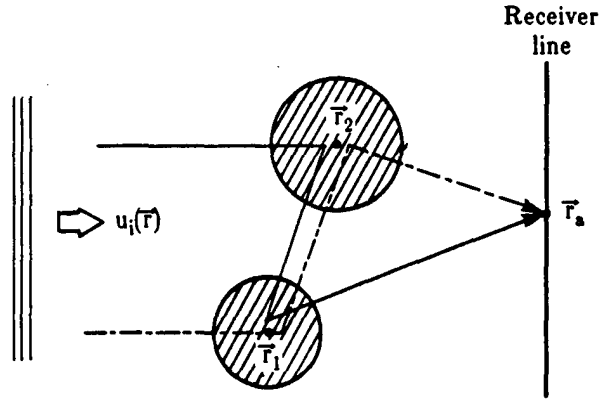

Fig. 25. This figure depicts the first and second-order scattered fields for a two component object.

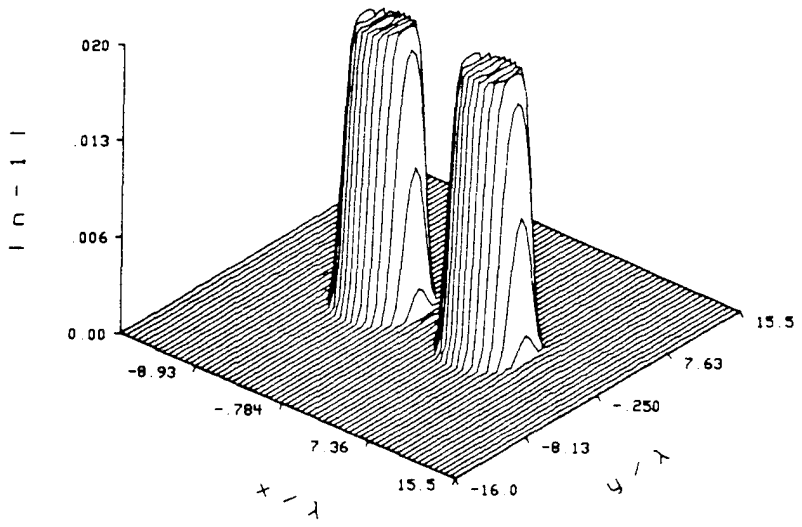

(a)

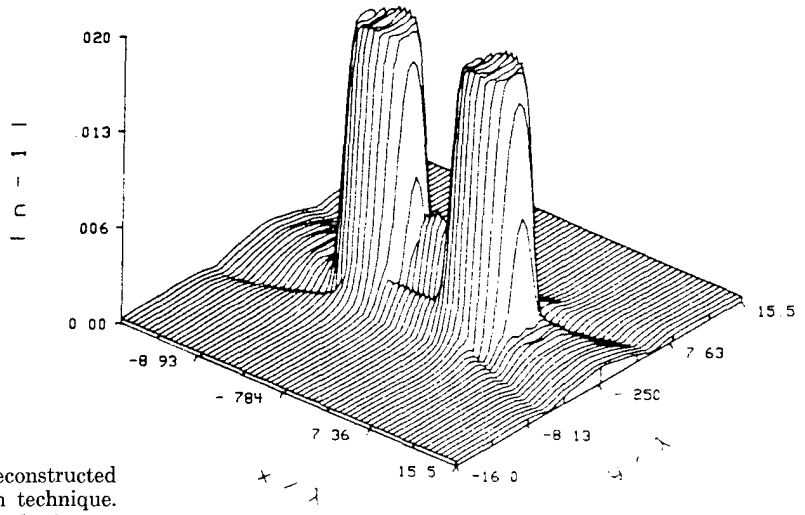

(b)

Fig. 26. Cross section of a two-component object reconstructed using the conventional diffraction reconstruction technique. Diameter of the cylinders is 6λ and their refractive index is 1.02. (a) Only the first order scattered fields are used for generating the data for this reconstruction. (b) Doubly scattered fields are included in the projection data for this reconstruction.

In Fig. 25, we have shown the first and the second order scattering processes for a two component object. For the first order scattering, each component interacts independently with the incident illumination, being oblivious of the existence of the other. To compute the second order scattering terms, each component interacts with the fields sent in its direction by the other component, and so on.

The computing procedure discussed above was used to generate 64 projections over 360° for the object. An interpolation based algorithm was then used to reconstruct the object cross-section; the results follow.

In the reconstructions shown in Figs. 26, 27, 28, and 29 we have shown the magnitude of the deviation of the reconstructed refractive index from that of the background, which was assumed to be unity. Plots labeled (a) show the reconstruction obtained when the projections were generated by ignoring the second and higher order scattered fields. On the other hand, the plots labeled (b) show the reconstructions when the second order fields are included in the projections.

In Fig. 26 the change in the refractive index of the 6λ cylinders was set to 2%. Although there is some distortion introduced in the direction of the line joining the center of the cylinders, it is negligible. However, when the refractive

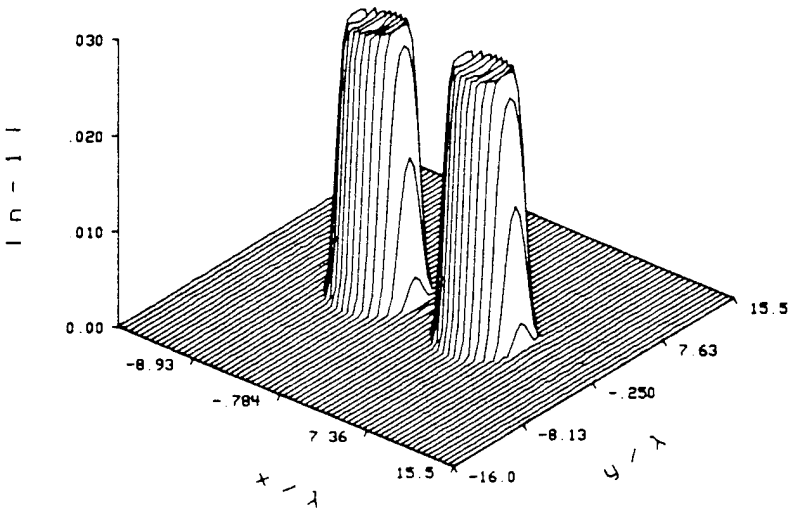

(a)

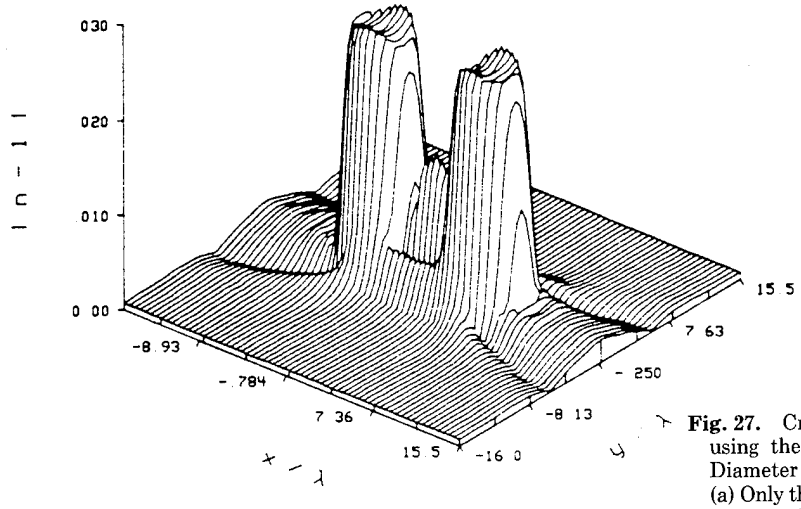

(b)

Fig. 27. Cross section of a two-component object reconstructed using the conventional diffraction reconstruction technique. Diameter of the cylinders is 6λ and their refractive index is 1.03. (a) Only the first order scattered fields are used for generating the data for this reconstruction. (b) Doubly scattered fields are included in the projection data for this reconstruction.

index change is increased in Fig. 27 to 3 percent, the distortion becomes quite noticeable; and in Fig. 28 a 5% change in refractive index is enough to cause the distortion to dominate the reconstruction. When the number of cylinders is increased the distortion is higher as seen in Fig. 29. This is expected because in this case there are more projections affected by second order scattering. It should be mentioned that the computational effort required for generating the projections is enormous. To illustrate, it took three hours of cpu time on the AP120B array processor for computing 64 projections of a three component object.

4.5 The Effect of Attenuation

Although in ultrasonic imaging the role of attenuation is minor, in microwave imaging it can not be ignored. Microwave attenuation rates in water are presented for the attenuation and phase factors at various frequencies in graphical and algebraic form by Foti *et al* elsewhere in this volume. Microwaves at 4 GHz, for example, undergo almost 3 db of attenuation per centimeter of travel in water; thus, the assumption in the Born approximation is quickly violated. In the remainder of this section, the effect of attenu-

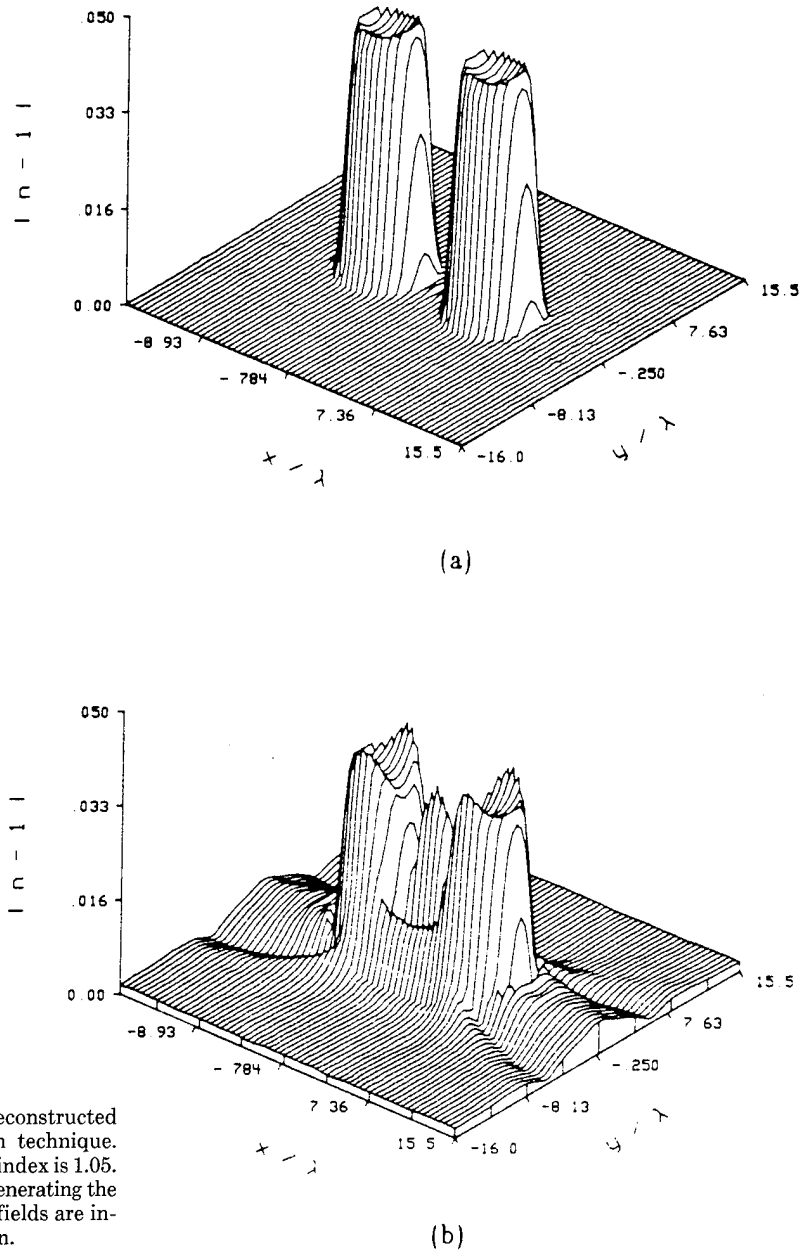

Fig. 28. Cross section of a two-component object reconstructed using the conventional diffraction reconstruction technique. Diameter of the cylinders is 6λ and their refractive index is 1.05. (a) Only the first order scattered fields are used for generating the data for this reconstruction. (b) Doubly scattered fields are included in the projection data for this reconstruction.

ation will be described as well as its affect on the resolution of the reconstruction.

The angular spectrum of a field on the line $x = x_1$ propagates to line $x = x_2$ according to the following relation

$$A(k_y,x_2) = A(k_y,x_1)e^{j\sqrt{k_0^2-k_y^2}(x_2-x_1)}. \quad (98)$$

Figure 30 shows a plot of the magnitude of the exponential factor in Eq. (98) as a function of both the attenuation of the medium and the spatial frequency of the plane wave in the y direction. We have plotted the magnitude in db as a function of the dimensionless parameter γ, where $k_x = \gamma k_0$. Thus, for $\gamma = 0$ the wave is traveling directly towards the receiver line, while for $\gamma = 1$ the wave is propagating along the direction of the receiver line. In this plot the attenuation factor and γ have been changed from 0 to 5.0 db/cm and 0 to 1.0, respectively. It is clear that the high frequency components (larger γ) are more attenuated than those components at lower frequencies (those that travel directly towards the receiver line). This means that as the field propagates in an attenuating medium, it loses its high frequency components.

Remembering the Fourier domain coverage of diffraction transmission tomography, one can now associate this phenomenon with a degradation in resolution. This point is illustrated in Fig. 31. As in the case of no attenuation, the inner circle corresponds to transmission tomography, while the outer ring represents the data measured by a reflection tomographic system. The difference made by attenua-

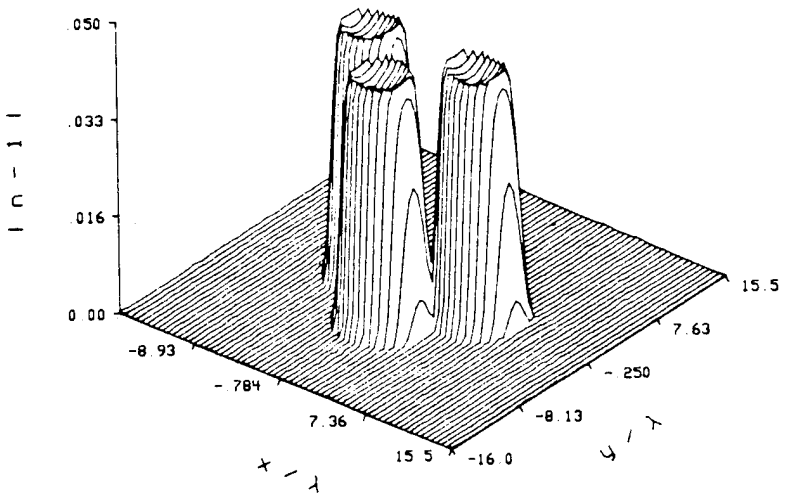

(a)

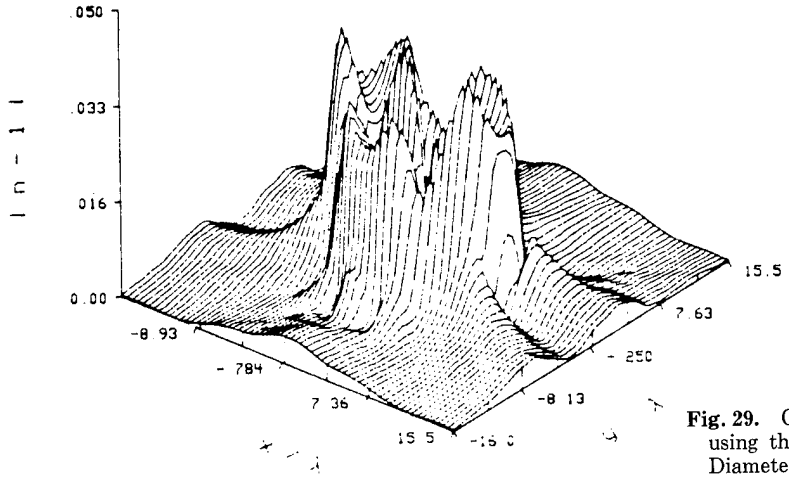

(b)

Fig. 29. Cross section of a two-component object reconstructed using the conventional diffraction reconstruction technique. Diameter of the cylinders is 6λ and their refractive index is 1.05. (a) Only the first order scattered fields are used for generating the data for this reconstruction. (b) Doubly scattered fields are included in the projection data for this reconstruction.

tion is shown as the shaded area. In this region, the attenuation of the medium reduces the amplitude of the plane wave components below a minimum tolerable Signal to Noise Ratio (SNR). Thus, this region of the object's Fourier transform is unmeasurable.

In the Synthetic Aperture technique, the concept of propagation of the angular spectrum can be applied in an attenuating medium. This results in upper bounds on k_y and β. k_y is the spatial frequency associated with the transmitter, and β is the spatial frequency associated with the receiver. This point is illustrated in Fig. 32. More angular views restore the resolution lost due to the use of an attenuating coupling medium. The coverage in the reflection mode also shrinks as shown in the figure.

5. CONCLUSIONS

The use of microwave tomographic imaging gives the physician new information about the physiologic status of a patient. X-ray tomography is based on the Fourier Slice Theorem; but, because of the diffraction and refraction of microwaves as they travel through the body, this theory is not useful with microwaves. Instead the Fourier Diffraction Projection Theorem is used to relate the fields scattered by an object illuminated with a plane wave to the Fourier transform of the object. Like the x-ray case, it is possible to measure the scattered fields from a number of different directions and form an estimate of the object's microwave refractive index.

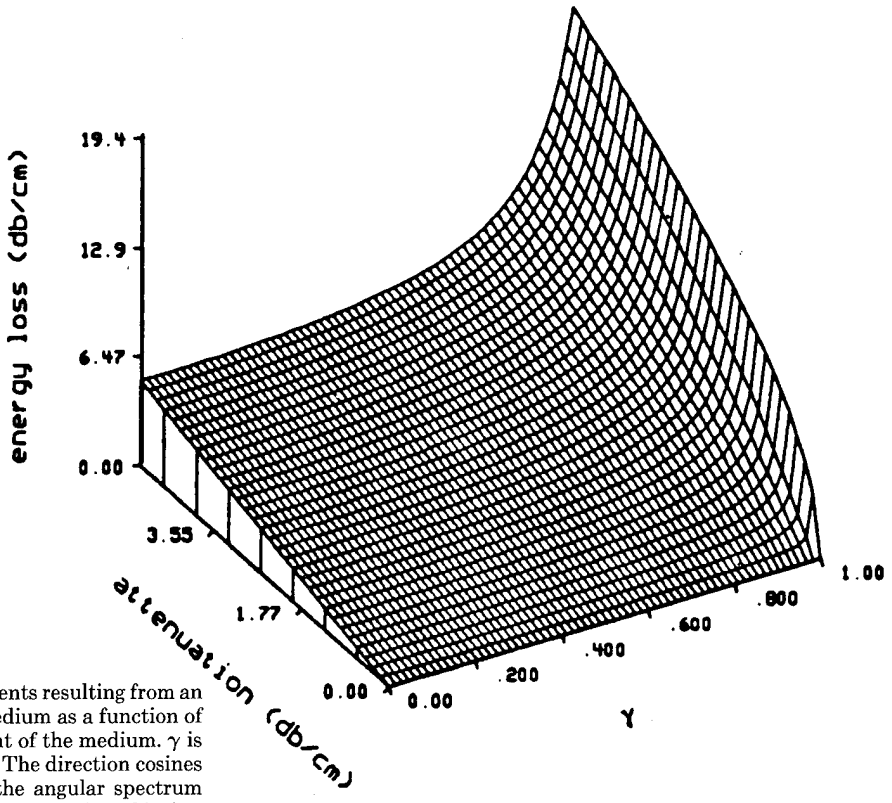

Fig. 30. Energy loss of plane wave components resulting from an angular spectrum expansion in a lossy medium as a function of directional angle and attenuation constant of the medium. γ is the direction cosine of these components. The direction cosines are related to the spatial frequency of the angular spectrum components as described by Goodman (27, sect. 3.8), and in Appendix I of the paper by Farhat elsewhere in this volume.

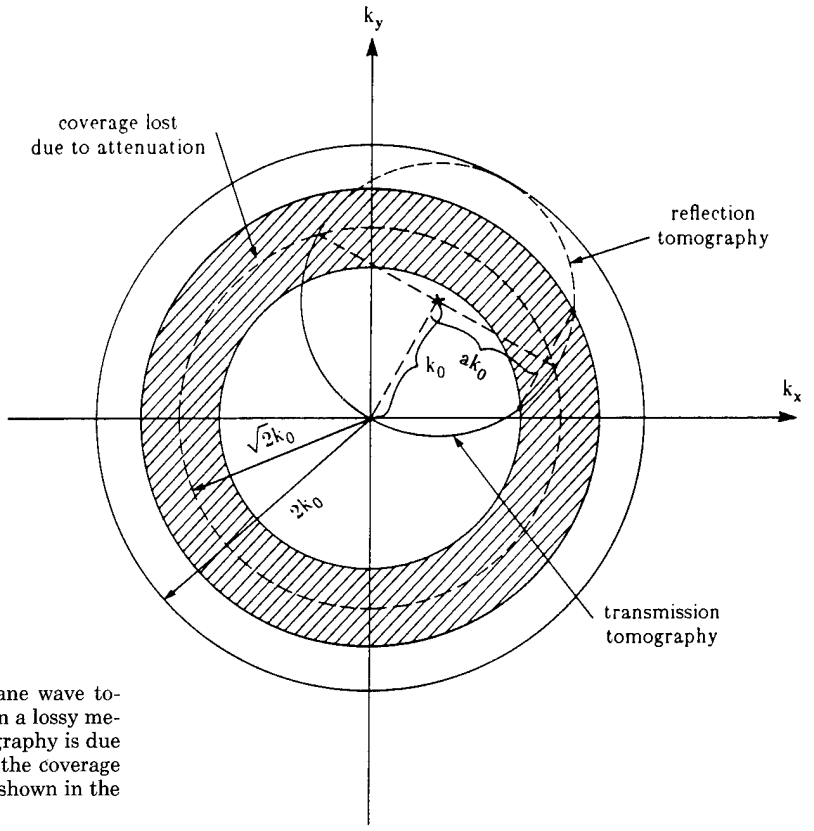

Fig. 31. Object's Fourier domain coverage for plane wave tomography in transmission and reflection modes, in a lossy medium. The lower resolution in transmission tomography is due to the smaller radius ($\sqrt{2}k_0$ compared to $2k_0$) of the coverage circle as shown here. The effect of attenuation is shown in the shaded area.

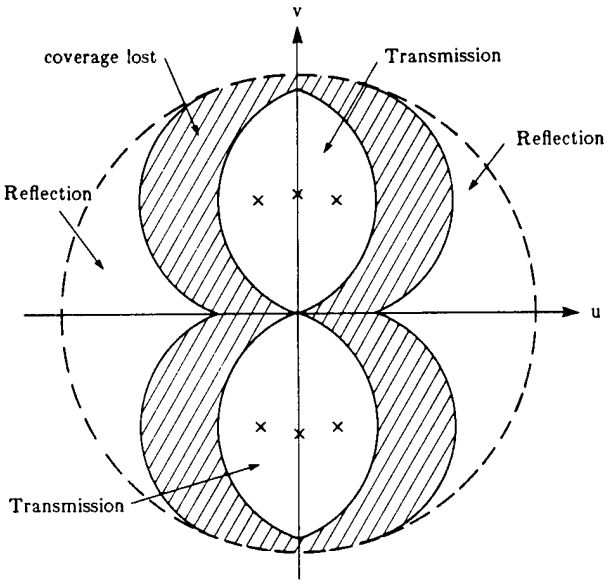

Fig. 32. When the medium is lossy, a larger number of views in the Synthetic Aperature technique can increase the resolution and decrease the distortion in the reconstructed image. The coverage shown corresponds to three rotational views of the object, 60° apart.

In addition, this chapter has presented an alternative derivation of the Fourier Diffraction Projection Theorem. This approach will allow for efficient implementations of higher order reconstruction techniques on digital computers.

By carefully designing a simulation procedure, we have isolated the effects of the first order Born and Rytov approximations in diffraction imaging. While both procedures can produce excellent reconstructions for small objects with small refractive index changes, they both quickly break down when their assumptions are violated. The assumptions limit the Born approximation to objects where the product of the diameter and the relative refractive index are less than 0.35λ; and the Rytov approximation to objects with a refractive index that differs by less than 2% from the surrounding media, with essentially no constraint on the size of the object.

Two problems need to be solved for microwave imaging to become successful for medical imaging. Foremost, reconstruction algorithms based on higher order approximations to the scattered field will be needed. With 4 GHz microwaves in water, biological structures span tens of wavelengths and often have refractive index variations of more than 100%. In addition, high spatial frequency suffer from large attenuation in water-based microwave systems. An approach that takes into account the attenuation effects of the coupling medium and the target should be studied. Microwave systems for medical imagery must take into account the different Fourier coverage provided by S_{11} and S_{21} data collection system designs and seek high k coupling media with lower loss.

References

1. L. E. Larsen and J. H. Jacobi, "Microwave scattering parameter imagery of an isolated canine kidney," *Med. Phys.*, Vol. 6, pp. 394–403, Sep./Oct., 1979.
2. L. E. Larsen, J. H. Jacobi, and A. K. Krey, "Preliminary observations with an electromagnetic method for the noninvasive analysis of cell suspension physiology and induced pathophysiology," *IEEE Trans. Microwave Theory Tech.*, Vol. MTT-26, pp. 581–595, Aug., 1978.
3. L. E. Larsen and J. H. Jacobi, "Microwave interrogation of dielectric targets: Part 1: By scattering parameters," *Med. Phys.*, Vol. 5, pp. 500–508, Nov./Dec., 1978.
4. O. C. Yue, E. L. Rope, and G. Tricoles, "Two reconstruction methods for microwave imaging of buried dielectric anomaly," *IEEE Trans. Comput.*, Vol. C-24, pp 381–390, Apr., 1975.
5. Loris B, Gregoris and Keigo Iizuka, "Visualization of internal structure by microwave holography," *Proc. IEEE*, Vol. 594, pp. 791–792, May, 1970.
6. A. Rosenfeld and A. C. Kak, *Digital Picture Processing*, Academic Press, Second Edition, 1982.
7. A. H. Andersen and A. C. Kak, "Simultaneous algebraic reconstruction technique (SART): A superior implementation of the ART algorithm," *Ultrason. Imag.*, Vol. 6, pp. 81–94, Jan., 1984.
8. A. H. Andersen and A. C. Kak, "Digital ray tracing in two-dimensional refractive fields," *J. Acoust. Soc. Am.*, Vol. 72, pp. 1593–1606, Nov., 1982.
9. A. J. Devaney, "A filtered backpropagation algorithm for diffraction tomography," *Ultrason. Imag.*, Vol. 4, pp. 336–350, 1982.
10. A. C. Kak, "Tomographic imaging with diffracting and non-diffracting sources," in *Array Signal Processing*, Simon Haykin, ed., Prentice Hall, 1984.
11. R. K. Mueller, M. Kaveh, and G. Wade, "Reconstructive tomography and applications to ultrasonics," *Proc. IEEE*, Vol. 67, pp. 567–587, 1979.
12. E. Wolf, "Three-dimensional structure determination of semi-transparent objects from homographic data," *Opt. Commun.*, Vol. 1, pp. 153–156, 1969.
13. S. X. Pan and A. C. Kak, "A computational study of reconstruction algorithms for diffraction tomography: Interpolation vs. filtered-backpropagation," *IEEE Trans. Acous. Speech Signal Process.*, pp. 1262–1275, Oct., 1983.
14. K. Iwata and R. Nagata, "Calculation of refractive index distribution from interferograms using the Born and Rytov's approximations," *Jap. J. Appl. Phys.*, Vol. 14, pp. 1921–1927, 1975.
15. A. Ishimaru, *Wave Propagation and Scattering in Random Media*, Academic Press, New York, 1978.
16. Philip M. Morse and Herman Feshbach, *Methods of Theoretical Physics*, McGraw Hill Book Company, New York, 1953.
17. L. A. Chernov, *Wave Propagation in a Random Medium*, McGraw Hill Book Company, New York, 1960.
18. J. B. Keller, "Accuracy and validity of the Born and Rytov approximations," *J. Opt. Soc. Am.*, Vol. 59, pp. 1003–1004, 1969.
19. S. K. Kenue and J. F. Greenleaf, "Limited angle multifrequency diffraction tomography," *IEEE Trans. Sonics Ultrason.*, Vol. SU-29, pp. 213–217, July, 1982.
20. William H. Carter, "Computational reconstruction of scattering objects from holograms," *J. Opt. Soc. Am.*, Vol. 60, pp. 306–314, March, 1970.
21. W. H. Carter and P. C. Ho, "Reconstruction of inhomogeneous scattering objects from holograms," *Appl. Opt.*, Vol. 13, pp. 162–172, Jan., 1974.

22. P. L. Carson, T. V. Oughton, and W. R. Hendee, "Ultrasound transaxial tomography by reconstruction," in *Ultrasound in Medicine II*, D. N. White and R. W. Barnes, eds., Plenum Press, pp. 391–400, 1976.
23. M. Kaveh, M. Soumekh, and R. K. Mueller, "Tomographic imaging via wave equation inversion," *ICASSP 82*, pp. 1553–1556, May, 1982.
24. D. Nahamoo and A. C. Kak, *Ultrasonic diffraction imaging*, TR-EE 82-20, School of Electrical Engineering, Purdue University, 1982.
25. D. Nahamoo, S. X. Pan, and A. C. Kak, "Synthetic aperture diffraction tomography and its interpolatioin-free computer implementation," *IEEE Trans. Sonics Ultrason.*, Vol. SU-31, pp. 218–229, July, 1984.
26. A. J. Devaney, "Geophysical diffraction tomography," *IEEE Trans. Geo. Sci., Special Issue Remote Sensing*, Vol. GE-22, pp. 3–13, Jan., 1984.
27. J. W. Goodman, *Introduction to Fourier Optics*, McGraw Hill Book Company, San Francisco, 1968.
28. M. Soumekh, M. Kaveh, and R. K. Mueller, "Fourier domain reconstruction methods with application to diffraction tomography," *Acoust. Imaging*, Vol. 13, pp. 17–30, 1984.
29. M. Soumekh and M. Kaveh, "Image reconstruction from frequency domain data on arbitrary contours," *Int. Conf. Acoust. Speech and Signal Process.*, pp. 12A.2.1–12A.2.4, 1984.
30. S. D. Conte and C. deBoor, *Elementary Numerical Analysis*, McGraw-Hill, New York, 1980.
31. Josef Stoer and Roland Bulirsch, *Introduction to Numerical Analysis*, Springer-Verlag, New York, 1980.
32. F. S. Acton, *Numerical Methods that Work*, Harper & Row, New York, 1970.
33. Malcolm Slaney and A. C. Kak, "Diffraction tomography," *Proc. SPIE*, vol. 413, pp. 2–19, Apr., 1983.
34. Malcolm Slaney and A. C. Kak, *Imaging with Diffraction, Tomography*, TR-EE 85-5, School of Electrical Engineering, Purdue University, March, 1985.
35. W. L. Weeks, *Electromagnetic Theory for Engineering Applications*, John Wiley and Sons, Inc., New York, 1964.
36. M. Azimi and A. C. Kak, "Distortion in diffraction imaging caused by multiple scattering," *IEEE Trans. Med. Imag.*, Vol. MI-2, pp. 176–195, Dec., 1983.